PHYSICAL REVIEW D **92,** 094019 (2015)

Nucleon resonances with spin $3/2$ and $5/2$ in the isobar model for kaon photoproduction

T. Mart, S. Clymton, and A. J. Arifi

Departemen Fisika, FMIPA, Universitas Indonesia, Depok 16424, Indonesia

(Received 10 April 2015; published 18 November 2015)

We compare two different propagator and vertex factor formulations of spin-$3/2$ and $-5/2$ nucleon resonances by using isobar models for kaon photoproduction on the proton $\gamma + p \to K^+ + \Lambda$. All nucleon resonances listed in the Particle Data Group listing with spin up to $5/2$ and with at least a two-star rating are included in the model. The unknown coupling constants are extracted from fitting to around 7400 data points. It is found that the gauge-invariant formulation of the spin-$3/2$ and $-5/2$ interactions leads to a better agreement with experimental data. An extensive comparison of model calculation with experimental data and comparison with the previous analyses are presented. A short discussion on the cross section near the production threshold is also provided.

DOI: 10.1103/PhysRevD.92.094019 PACS numbers: 13.60.Le, 14.20.Gk, 25.20.Lj

I. INTRODUCTION

The existence of abundant kaon photo- and electroproduction data obtained from continuous electron beam accelerators combined with modern high-resolution detectors in the last two decades indicates the enormous advances in the investigation of strangeness physics. These accurate data obviously deserve modern and sophisticated analyses by means of the model that is not only containing as much as possible physics ingredients but also able to accurately reproduce the data. Achieving the two objectives simultaneously would be a daunting task, because imposing more physics constraints on the model would commonly worsen the agreement between model calculation and experimental data.

Meanwhile, substantial achievements have been also made on the theoretical side. A number of coupled-channels calculations have included kaon photo and electroproduction channels in their fits [1,2]. The advantage of the coupled-channels formalism is clear, since within this formalism all related reactions can be simultaneously analyzed in a unified and more consistent framework. However, to achieve a very good agreement with experimental data for a certain channel, e.g., the kaon photoproduction channel, is not easy within this framework, especially because the kaon photoproduction is not the dominant channel in this case (see Figs. 37–45 of Ref. [1], for instance).

A single-channel analysis is certainly simpler and easier to perform. Although with the risk of destroying the unitarity of the scattering amplitude, by using a single-channel analysis, one can easily investigate any structure appearing in the differential and total cross section [3] or other observables [4,5]. The unitarity in this tree-level calculation could be partly restored by imposing an energy-dependent width [6], in which the required relative branching ratios can be obtained from the latest Review of Particle Properties of the Particle Data Group (PDG) [7] or the results from previous coupled-channel calculations [1,2]. Furthermore, the elementary operator obtained from the single-channel analysis is very useful and practical for applications in the hypernuclear physics [8], kaon photoproduction on a deuteron [9], or other related phenomenological studies [10]. Obviously, an accurate elementary operator is a prerequisite for a reliable prediction of the hypernuclear production observables.

Despite its simplicity, the single-channel analysis is also plagued with some notorious problems. One of them is the large number of nucleon and hyperon resonances that are involved in the process, whereas the corresponding coupling constants and hadronic form factors are hardly known. In the energy range from threshold up to 2.8 GeV, where most of the experimental data exist, there exist 26 nucleon resonances and 19 hyperon resonances as listed by PDG [7]. There has been a new strategy to overcome this problem, i.e., by using the Bayesian inference method [11]. However, the analysis has been only performed in a single-channel analysis of kaon photoproduction and by excluding the resonances with the mass below the production threshold and those with spin higher than $5/2$. As is pointed out in Ref. [11], the nature of the background terms in this reaction is also a delicate problem. There is no unique procedure to determine the background terms in the single-channel analysis, whereas in the coupled channels one, the background terms of one channel are strongly connected to other channels.

In this paper, we aim to study the effects of using different models for spin-$3/2$ and $-5/2$ nucleon resonances in the $\gamma + p \to K^+ + \Lambda$ photoproduction process. This study is primarily motivated by our experience that it is difficult to simultaneously fit the presently available experimental data by using the amplitudes for spin-$3/2$ and $-5/2$ nucleon resonances obtained from the propagator and

vertex factors given in Refs. [12,13]. Since the problem of a consistent spin-3/2 propagator has generated considerable discussion in the literature [14–20], comparison with other prescriptions of the propagator is certainly of interest. Furthermore, the spin-3/2 prescription given in Refs. [12,13] has received a number of criticisms in the literature [17–20].

It is clear that the various versions of the spin-3/2 propagator will reduce to the Rarita–Schwinger form [14] in the case of an on-shell baryon. In the case of an off-shell baryon, Ref. [17] pointed out that a correct form of the spin-3/2 propagator amounts for additional explicit off-shell terms. Meanwhile, Ref. [21] obtained that a correct gauge-invariant coupling chosen in the model leads to a consistent spin-3/2 theory that removes the so-called "spin-1/2 background." Put in other words, a consistent interaction should not activate the extra unphysical degrees of freedom [22]. In this paper, we use this prescription in Model 2, whereas Model 1 utilizes the method developed in Refs. [12,13]. We note that the prescription of Ref. [21] has been also extended to the spin-5/2 case [20].

There have been attempts to compare the effects of different propagator prescriptions in the kaon photoproduction. Reference [18], e.g., has reported that the inclusion of off-shell terms leads to a small effect, whereas Ref. [19] found that the propagator choice has a small effect and is only sizable for certain polarization observables. In this paper, however, we obtain a different result. The use of the propagator and vertex factors constructed in a gauge-invariant fashion [16,21,22] results in a much better agreement with the experimental data. Note that in this investigation we use a significantly larger database than that of Ref. [19].

The organization of this paper is as follows. In Sec. II, we describe the ingredient of our isobar model. In Sec. III, we present the different prescriptions of propagator and vertex factors of spin-3/2 and −5/2 nucleon resonances used in our calculation. Section IV explains the energy-dependent width used in our calculation. The numerical result as well as comparison of our calculation with experimental data are given in Sec. V. In Sec. VI, we compare the calculated observables obtained in the present work with those obtained from previous analyses. Comparison of the calculated Chew-Goldberger-Low-Nambu (CGLN) amplitudes and multipoles is presented in Sec. VII. Finally, in Sec. VIII, we summarize our discussion and conclude our finding. The calculated amplitudes for spin-3/2 and −5/2 nucleon resonances are given in Appendixes A and B.

II. ISOBAR MODEL

We consider the elementary process for the electroproduction of a kaon and a hyperon on a nucleon target,

$$e(k_{\rm i}) + p(p) \to e'(k_{\rm f}) + K^+(q) + \Lambda(p_\Lambda), \qquad (1)$$

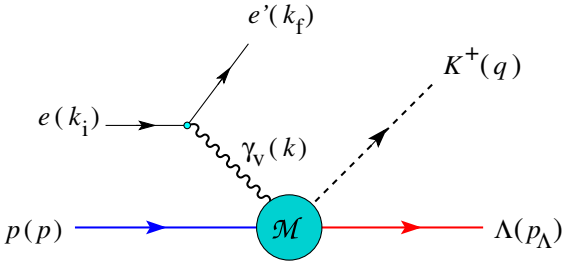

FIG. 1 (color online). Kinematics of the kaon electroproduction process $e + p \to e' + K^+ + \Lambda$. The process can be also considered as a virtual kaon photoproduction, i.e., kaon photoproduction by the virtual photon $\gamma_{\rm v}$.

which is depicted in Fig. 1. The production amplitude $\mathcal{M}$ can be modeled by using the appropriate Feynman diagrams as shown in Fig. 2.

The formulation of this process is equivalent to that of the virtual photoproduction, i.e., the photoproduction by a virtual photon,

$$\gamma_{\rm v}(k) + p(p) \to K^+(q) + \Lambda(p_\Lambda), \qquad (2)$$

with $k = k_{\rm i} - k_{\rm f}$. The following calculation is performed by using the latter, where in general $k^2 \neq 0$. However, the present analysis will focus on the photoproduction process. For the sake of completeness, as well as for our future studies on kaon electroproduction, we will in this paper prepare the general electroproduction formulation, where the photoproduction reaction is only a special case with $k^2 = 0$. Since in the present analysis we will only focus on the photoproduction, we will, for the sake of brevity, exclude the electromagnetic form factors of the nucleon resonance. Later, for the electroproduction case, these form factors can be simply inserted in the resonance coupling constants.

Following the convention of Refs. [23,24], we can decompose the scattering amplitude obtained from the Feynman diagrams shown in Fig. 2 into the gauge and Lorentz invariant matrices M_i,

$$\begin{aligned}\mathcal{M} &= \mathcal{M}_{\rm back} + \mathcal{M}_{\rm res} \\ &= \bar{u}_\Lambda \sum_{i=1}^{6} A_i(s,t,u,k^2) M_i u_p, \end{aligned} \qquad (3)$$

where we have separated the background and resonance contributions to the scattering amplitude explicitly and $\bar{u}_\Lambda = \bar{u}(p_\Lambda)$ and $u_p = u(p)$ are the Λ and proton spinors in the final and initial states, respectively. The Mandelstam variables, s, t, and u, are defined by

$$s = (k+p)^2 = W^2, \qquad (4)$$

$$t = (k-q)^2, \qquad (5)$$

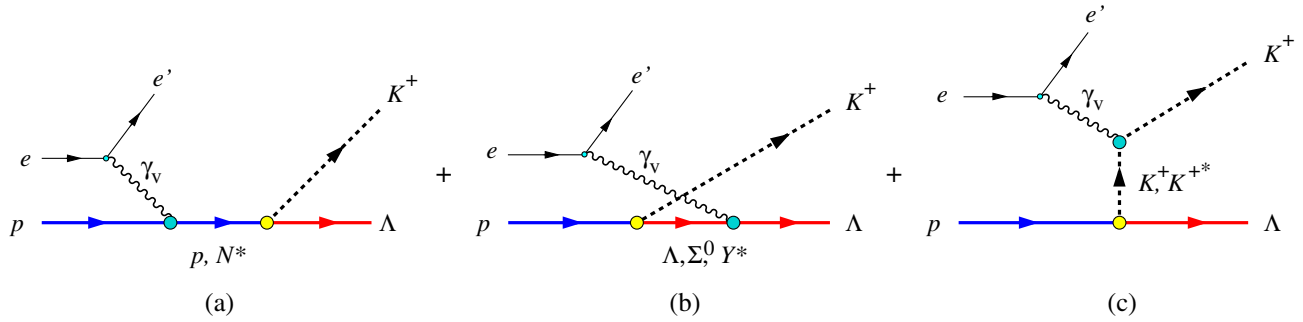

FIG. 2 (color online). Feynman diagrams for the elementary operator of the kaon electroproduction process $e + p \to e' + K^+ + \Lambda$. The intermediate states in these diagrams are (a) the s-channel proton and nucleon resonances; (b) the u-channel Λ, Σ^0, and hyperon resonances; and (c) the t-channel kaon and kaon resonances.

$$u = (k - p_\Lambda)^2. \tag{6}$$

The gauge and Lorentz invariant matrices M_i are given by [23,24]

$$M_1 = \frac{1}{2}\gamma_5(\not\epsilon\not k - \not k\not\epsilon), \tag{7}$$

$$M_2 = \gamma_5[(2q - k)\cdot\epsilon P\cdot k - (2q - k)\cdot kP\cdot\epsilon], \tag{8}$$

$$M_3 = \gamma_5(q\cdot k\not\epsilon - q\cdot\epsilon\not k), \tag{9}$$

$$M_4 = i\epsilon_{\mu\nu\rho\sigma}\gamma^\mu q^\nu\epsilon^\rho k^\sigma, \tag{10}$$

$$M_5 = \gamma_5(q\cdot\epsilon k^2 - q\cdot k k\cdot\epsilon), \tag{11}$$

$$M_6 = \gamma_5(k\cdot\epsilon\not k - k^2\not\epsilon), \tag{12}$$

where γ_μ is the Dirac matrix and throughout this paper we have used the notation of Bjorken and Drell [25], i.e., $\not p = p_\mu\gamma^\mu$, $2g_{\mu\nu} = \gamma^\mu\gamma^\nu + \gamma^\nu\gamma^\mu$, $g_{\mu\nu} = \mathrm{diag}(1,-1,-1,-1)$. Furthermore, in Eq. (8), we have also defined $P = \frac{1}{2}(p + p_\Lambda)$, and in Eq. (10), $\epsilon_{\mu\nu\rho\sigma}$ is the four-dimensional Levi-Civitá tensor with $\epsilon_{0123} = +1$. Note that for photoproduction, in the transverse gauge $\epsilon\cdot k = k^2 = 0$, only the matrices M_1 to M_4 contribute. The cross section and other polarization observables can be calculated from the amplitudes A_i [26–28].

All intermediate states that contribute to this process are symbolically depicted in Fig. 2. Based on our previous studies [3,29–36], the background terms consist of the standard s-, u-, and t-channel Born terms along with the $K^{*+}(892)$ and $K_1(1270)$ t-channel vector mesons. Two hyperon resonances that have been found to be important to maintain a reasonable value of the hadronic form factor cutoff of the Born terms [32] are also included.

Since both the baryon and meson are not pointlike particles, we have to account for the hadronic structures of interacting baryons and mesons. For this purpose, we include the hadronic form factors in the hadronic vertices by adopting the method developed by Haberzettl to maintain the gauge invariance of the amplitudes [37]. By writing x as the Mandelstam variables s, t, and u, the form factor reads

$$F(\Lambda, x) = \frac{\Lambda^4}{\Lambda^4 + (x - m^2)^2}, \tag{13}$$

where Λ and m are the form factor cutoff and the intermediate state mass, respectively [37]. We also note that this method introduces two more free parameters which come from the freedom of the form factor for the electric amplitude A_2 [see Eq. (3)]. To this end, the form factor can be written as [37]

$$\begin{aligned}\tilde F = {} & F(\Lambda, s)\sin^2\theta_{\mathrm{had}}\cos^2\phi_{\mathrm{had}} \\ & + F(\Lambda, u)\sin^2\theta_{\mathrm{had}}\sin^2\phi_{\mathrm{had}} \\ & + F(\Lambda, t)\cos^2\theta_{\mathrm{had}},\end{aligned} \tag{14}$$

where the combination of sinusoidal functions ensures the correct normalization of the form factor. Both θ_{had}. and ϕ_{had}. are obtained from the fit.

For the nucleon resonances, we include all nucleon resonances listed by the 2014 PDG listing [7] with the status at least a two-star rating and having spin up to 5/2. Their masses, widths, and status are listed in Table I.

We note that the formulation for the nucleons and hyperons with spin 1/2, as well as that of the mesons with spin 0 and 1, have been well established. Therefore, in the present paper, we will not discuss this issue in detail. Instead, we will only refer the reader to Refs. [12,13] for a good discussion to this end. As previously discussed in the Introduction, this is, however, not the case for spin-3/2 and −5/2 baryons, for which two models of nucleon resonances with spin 3/2 and 5/2 are the main topic of discussion in the present paper and the formulation of their amplitudes will be given in Sec. III.

TABLE I. The status, mass, and width of the resonances used in our calculation [7].

Resonance	Status [a]	Mass (MeV)	Width (MeV)
$N(1440)P_{11}$	****	1430 ± 20	350 ± 100
$N(1520)D_{13}$	****	1515 ± 5	115^{10}_{-15}
$N(1535)S_{11}$	****	1535^{+20}_{-10}	150 ± 25
$N(1650)S_{11}$	****	1655^{+15}_{-10}	140 ± 30
$N(1675)D_{15}$	****	1675 ± 5	150^{+15}_{-20}
$N(1680)F_{15}$	****	1685 ± 5	130 ± 10
$N(1700)D_{13}$	***	1700 ± 50	150^{+100}_{-50}
$N(1710)P_{11}$	***	1710 ± 30	100^{+150}_{-50}
$N(1720)P_{13}$	****	1720^{+30}_{-20}	250^{+150}_{-100}
$N(1860)F_{15}$	**	1860^{+100}_{-40}	270^{+140}_{-50} [b]
$N(1875)D_{13}$	***	1875^{+45}_{-55}	200 ± 25 [b]
$N(1880)P_{11}$	**	1870 ± 35 [b]	235 ± 65
$N(1895)S_{11}$	**	1895 ± 15 [b]	90^{+30}_{-15}
$N(1900)P_{13}$	***	1900	250
$N(2000)F_{15}$	**	2050 ± 100	198 ± 2 [b]
$N(2060)D_{15}$	**	2060	375 ± 25
$N(2120)D_{13}$	**	2120	330 ± 45 [b]

[a]Status according to the PDG [7].
[b]Estimated value taken from a reference listed in PDG.

III. MODELS FOR THE SPIN-3/2 AND SPIN-5/2 NUCLEON RESONANCES

A. Model 1

1. Spin-3/2 in Model 1

In Model 1, we follow the formulation of the spin-3/2 propagator, the electromagnetic and hadronic vertices, as given in Ref. [12]. This formulation was also adopted by Ref. [13]. In this formulation, the spin-3/2 propagator is written as

$$P^{3/2}_{\mu\nu} = \frac{\not{p} + \not{k} + \sqrt{s}}{3(s - m^2_{N^*} + i m_{N^*}\Gamma_{N^*})} \times \left[g_{\mu\nu} + \gamma_\nu\gamma_\mu - \frac{2}{s}(p+k)_\mu (p+k)_\nu - \frac{1}{\sqrt{s}}\{\gamma_\mu (p+k)_\nu - \gamma_\nu (p+k)_\nu\}\right]. \quad (15)$$

The electromagnetic $N^* p\gamma$ vertex for the nucleon resonance with parity ± 1 reads

$$\Gamma^{\nu(\pm)}_{N^* p\gamma} = \left\{ g^a_{N^* p\gamma}\left(\epsilon^\nu - \frac{\not{\epsilon} k^\nu}{\sqrt{s} \pm m_p}\right) + g^b_{N^* p\gamma}\frac{p\cdot\epsilon k^\nu - p\cdot k\epsilon^\nu}{(\sqrt{s}\pm m_p)^2} + g^c_{N^* p\gamma}\frac{k\cdot\epsilon k^\nu - k^2\epsilon^\nu}{(\sqrt{s}\pm m_p)^2}\right\}\Gamma_\pm, \quad (16)$$

where $\Gamma_+ = i\gamma_5$ and $\Gamma_- = 1$ [13]. Note that the last term in Eq. (16) represents the longitudinal contribution of this vertex [38].

In the case of electroproduction, the first term in Eq. (16) is not explicitly gauge invariant. To this end, we can impose the gauge transformation [13]

$$\epsilon^\nu \to \epsilon^\nu - (k\cdot\epsilon/k^2)k^\nu \quad (17)$$

on Eq. (16), which only modifies the first term, i.e.,

$$\epsilon^\nu - \frac{\not{\epsilon} k^\nu}{\sqrt{s}\pm m_p} \to \frac{1}{k^2}\left\{ (k^2\epsilon^\nu - k\cdot\epsilon k^\nu) - \frac{1}{\sqrt{s}\pm m_p}(k^2\not{\epsilon} - k\cdot\epsilon\not{k})k^\nu\right\}. \quad (18)$$

Therefore, the gauge-invariant electromagnetic vertex has the form of

$$\Gamma^{\nu(\pm)}_{N^* p\gamma} = \left[\frac{g^a_{N^* p\gamma}}{k^2}\left\{(k^2\epsilon^\nu - k\cdot\epsilon k^\nu) - \frac{1}{\sqrt{s}\pm m_p}(k^2\not{\epsilon} - k\cdot\epsilon\not{k})k^\nu\right\} + g^b_{N^* p\gamma}\frac{p\cdot\epsilon k^\nu - p\cdot k\epsilon^\nu}{(\sqrt{s}\pm m_p)^2} + g^c_{N^* p\gamma}\frac{k\cdot\epsilon k^\nu - k^2\epsilon^\nu}{(\sqrt{s}\pm m_p)^2}\right]\Gamma_\pm. \quad (19)$$

The hadronic vertex is simpler than the electromagnetic one because we use the pseudoscalar theory that nicely works in the case of kaon photoproduction [30]. The vertex reads

$$\Gamma^{\mu(\pm)}_{K\Lambda N^*} = \frac{g_{K\Lambda N^*}}{m_{N^*}} p^\mu_\Lambda \Gamma_\mp. \quad (20)$$

Hence, the amplitude for spin-3/2 nucleon resonance with parity ± 1 can be written as

$$\mathcal{M}^{3/2}_{\rm res} = \bar{u}_\Lambda \Gamma^\mu_{K\Lambda N^*} P_{\mu\nu}\Gamma^\nu_{N^* p\gamma} u_p = \mp\bar{u}_\Lambda\gamma_5 p^\mu_\Lambda(\not{p} + \not{k} \mp \sqrt{s})\left\{ g_{\mu\nu} + \gamma_\nu\gamma_\mu - \frac{2}{s}q_\mu q_\nu \pm \frac{1}{\sqrt{s}}(\gamma_\mu q_\nu - \gamma_\nu q_\mu)\right\}[\mathcal{G}_1\{(k^2\epsilon^\nu - k\cdot\epsilon k^\nu) \pm c_\pm(k^2\not{\epsilon} - k\cdot\epsilon\not{k})k^\nu\} + \mathcal{G}_2(p\cdot\epsilon k^\nu - p\cdot k\epsilon^\nu) + \mathcal{G}_3(k\cdot\epsilon k^\nu - k^2\epsilon^\nu)]u_p, \quad (21)$$

where

$$\mathcal{G}_1 = \frac{i g_{K\Lambda N^*} g^a_{N^* p\gamma}}{3 m_{N^*} k^2 (s - m^2_{N^*} + i m_{N^*}\Gamma_{N^*})}, \quad (22)$$

$$\mathcal{G}_2 = \frac{ig_{K\Lambda N^*} g^b_{N^* p\gamma} c_\pm^2}{3m_{N^*}(s - m_{N^*}^2 + im_{N^*}\Gamma_{N^*})}, \tag{23}$$

$$\mathcal{G}_3 = \frac{ig_{K\Lambda N^*} g^c_{N^* p\gamma} c_\pm^2}{3m_{N^*}(s - m_{N^*}^2 + im_{N^*}\Gamma_{N^*})}, \tag{24}$$

with $c_\pm \equiv 1/(\sqrt{s} \pm m_p)$.

By decomposing the amplitude in terms of the M_i matrices given in Eqs. (7)–(12),

$$\mathcal{M}^{3/2}_{\rm res} = \bar{u}_\Lambda \sum_{i=1}^{6} A_i M_i u_p, \tag{25}$$

we obtain the amplitudes $A_1, \ldots, A_6$ for the spin-3/2 nucleon resonance of Model 1 as shown by Eqs. (A1)–(A6) in Appendix A.

2. Spin 5/2 in Model 1

The propagator for spin-5/2 resonance in Model 1 is adopted from Ref. [13], i.e.,

$$\begin{aligned} P^{5/2}_{\mu\nu\alpha\beta} = & \frac{\not{p} + \not{k} + \sqrt{s}}{10(s - m_{N^*}^2 + im_{N^*}\Gamma_{N^*})} \\ & \times [5P_{\mu\alpha}P_{\nu\beta} - 2P_{\mu\nu}P_{\alpha\beta} + 5P_{\mu\beta}P_{\nu\alpha} \\ & + P_{\mu\rho}\gamma^\rho\gamma^\sigma P_{\sigma\alpha}P_{\nu\beta} + P_{\nu\rho}\gamma^\rho\gamma^\sigma P_{\sigma\beta}P_{\mu\alpha} \\ & + P_{\mu\rho}\gamma^\rho\gamma^\sigma P_{\sigma\beta}P_{\nu\alpha} + P_{\nu\rho}\gamma^\rho\gamma^\sigma P_{\sigma\alpha}P_{\mu\beta}], \end{aligned} \tag{26}$$

with

$$P_{\mu\nu} = -g_{\mu\nu} + \frac{1}{s}(p+k)_\mu (p+k)_\nu. \tag{27}$$

As in the case of the spin 3/2 [Eq. (19)], the modified electromagnetic vertex is [13,38]

$$\begin{aligned} \Gamma^{\alpha\beta(\pm)}_{N^* p\gamma} = & \left[\frac{g^a_{N^* p\gamma}}{k^2 m_{N^*}} \left\{ (k^2\epsilon^\alpha - k\cdot\epsilon k^\alpha)k^\beta \right.\right. \\ & \left. - \frac{1}{\sqrt{s} \pm m_p}(k^2 \not{\epsilon} - k\cdot\epsilon \not{k})k^\alpha k^\beta \right\} \\ & + \frac{g^b_{N^* p\gamma}}{m_{N^*}} \frac{(p\cdot\epsilon k^\alpha - p\cdot k\epsilon^\alpha)k^\beta}{(\sqrt{s} \pm m_p)^2} \\ & \left. + \frac{g^c_{N^* p\gamma}}{m_{N^*}} \frac{(k\cdot\epsilon k^\alpha - k^2\epsilon^\alpha)k^\beta}{(\sqrt{s} \pm m_p)^2} \right] \Gamma_\mp, \end{aligned} \tag{28}$$

whereas the hadronic vertex is

$$\Gamma^{\mu\nu(\pm)}_{K\Lambda N^*} = \frac{g_{K\Lambda N^*}}{m_{N^*}^2} p^\mu_\Lambda p^\nu_\Lambda \Gamma_\pm, \tag{29}$$

and the scattering amplitude can be decomposed into the M_i matrices as in the case of spin 3/2,

$$\begin{aligned} \mathcal{M}^{5/2}_{\rm res} &= \bar{u}_\Lambda \Gamma^{\mu\nu(\pm)}_{K\Lambda N^*} P_{\mu\nu\alpha\beta} \Gamma^{\alpha\beta(\pm)}_{N^* p\gamma} u_p \\ &= \pm \bar{u}_\Lambda \gamma_5 p^\mu_\Lambda p^\nu_\Lambda (\not{p} + \not{k} \pm \sqrt{s}) \{5P_{\mu\alpha}P_{\nu\beta} - 2P_{\mu\nu}P_{\alpha\beta} + 5P_{\mu\beta}P_{\nu\alpha} + P_{\mu\rho}\gamma^\rho\gamma^\sigma P_{\sigma\alpha}P_{\nu\beta} \\ &\quad + P_{\nu\rho}\gamma^\rho\gamma^\sigma P_{\sigma\beta}P_{\mu\alpha} + P_{\mu\rho}\gamma^\rho\gamma^\sigma P_{\sigma\beta}P_{\nu\alpha} + P_{\nu\rho}\gamma^\rho\gamma^\sigma P_{\sigma\alpha}P_{\mu\beta}\} [\mathcal{G}_1 \{(k^2\epsilon^\alpha - k\cdot\epsilon k^\alpha)k^\beta \\ &\quad \mp c_\mp (k^2 \not{\epsilon} - k\cdot\epsilon \not{k})k^\alpha k^\beta\} + \mathcal{G}_2 (p\cdot\epsilon k^\alpha - p\cdot k\epsilon^\alpha)k^\beta + \mathcal{G}_3 (k\cdot\epsilon k^\alpha - k^2\epsilon^\alpha)k^\beta] u_p \\ &= \bar{u}_\Lambda \sum_{i=1}^{6} A_i M_i u_p, \end{aligned} \tag{30}$$

where

$$\mathcal{G}_1 = \frac{ig_{K\Lambda N^*} g^a_{N^* p\gamma}}{10m^3_{N^*} k^2 (s - m_{N^*}^2 + im_{N^*}\Gamma_{N^*})}, \tag{31}$$

$$\mathcal{G}_2 = \frac{ig_{K\Lambda N^*} g^b_{N^* p\gamma} c_\mp^2}{10m^3_{N^*} (s - m_{N^*}^2 + im_{N^*}\Gamma_{N^*})}, \tag{32}$$

$$\mathcal{G}_3 = \frac{ig_{K\Lambda N^*} g^c_{N^* p\gamma} c_\mp^2}{10m^3_{N^*} (s - m_{N^*}^2 + im_{N^*}\Gamma_{N^*})}. \tag{33}$$

The result is given by Eqs. (A13)–(A18) in Appendix A.

B. Model 2

1. Spin 3/2 in Model 2

In this model, we choose the propagator of spin-3/2 nucleon resonance given in Ref. [21], which has a slightly different form compared to Model 1, i.e.,

$$\begin{aligned} P^{3/2}_{\mu\nu} = & \frac{\not{p} + \not{k} + m_{N^*}}{3(s - m_{N^*}^2 + im_{N^*}\Gamma_{N^*})} \\ & \times \left[-3g_{\mu\nu} + \gamma_\mu\gamma_\nu + \frac{1}{s}\{(\not{p} + \not{k})\gamma_\mu (p+k)_\nu \right. \\ & \left. + (p+k)_\mu \gamma_\nu (\not{p} + \not{k})\} \right], \end{aligned} \tag{34}$$

where $P_{\mu\nu}$ is given by Eq. (27).

The Lagrangian for the electromagnetic $N^*p\gamma$ vertex is given by [22]

$$\begin{aligned}\mathcal{L}_{N^*p\gamma} = \frac{1}{M^2}[&g^a_{N^*p\gamma}\tilde{G}_{\mu\nu} + g^b_{N^*p\gamma}\gamma_5 G_{\mu\nu} \\ &+ g^c_{N^*p\gamma}\gamma_\mu\gamma^\rho\tilde{G}_{\rho\nu} \\ &+ g^d_{N^*p\gamma}\gamma_5\gamma_\mu\gamma^\rho G_{\rho\nu}]F^{\mu\nu} + \text{H.c.},\end{aligned} \tag{35}$$

with $\tilde{G}_{\mu\nu} = \frac{1}{2}\epsilon_{\mu\nu\rho\sigma}G^{\rho\sigma} = \frac{1}{2}\epsilon_{\mu\nu\rho\sigma}(\partial^\rho\psi^\sigma - \partial^\sigma\psi^\rho)$ and $F^{\mu\nu}$ is the field strength tensor. From Eq. (35), we can construct the electromagnetic vertex factor, which in our notation is given by

$$\begin{aligned}\Gamma^\nu_{N^*p\gamma} = \frac{1}{m^2_{N^*}}[&g^a_{N^*p\gamma}\epsilon^{\nu\mu\rho\sigma}p_\sigma(k_\mu\epsilon_\rho - k_\rho\epsilon_\mu) \\ &+ g^b_{N^*p\gamma}\gamma_5(p\cdot k\epsilon^\nu - p\cdot\epsilon k^\nu) \\ &+ g^c_{N^*p\gamma}\epsilon^{\nu\mu\rho\sigma}p_\sigma(\not{k}\epsilon_\mu - \not{\epsilon}k_\mu)\gamma_\rho \\ &+ g^d_{N^*p\gamma}\gamma_5\{(\not{k}\not{p}\epsilon^\nu - \not{\epsilon}\not{p}k^\nu) \\ &- (p\cdot\epsilon\not{k} - p\cdot k\not{\epsilon})\gamma^\nu\}].\end{aligned} \tag{36}$$

This vertex factor is explicitly gauge invariant, i.e., $p_\mu\Gamma^\mu_{\text{e.m.}} = 0$ and $\Gamma^\mu_{\text{e.m.}}|_{\epsilon\to k} = 0$. Therefore, we do not need a gauge transformation for Eq. (36), as in the case of Model 1.

By exploiting the relation

$$i\epsilon^{\mu\nu\rho\sigma}\gamma_\mu = \gamma_5(-\gamma^\nu\gamma^\rho\gamma^\sigma + g^{\nu\rho}\gamma^\sigma + g^{\rho\sigma}\gamma^\nu - g^{\nu\sigma}\gamma^\rho), \tag{37}$$

we can simplify Eq. (36) to

$$\begin{aligned}\Gamma^{\nu(\pm)}_{N^*p\gamma} = -\frac{i}{m^2_{N^*}}[&g^{(1)}(\epsilon^\nu\not{k} - k^\nu\not{\epsilon})\not{p} \\ &+ g^{(2)}(k^\nu p\cdot\epsilon - \epsilon^\nu p\cdot k) \\ &+ g^{(3)}p^\nu(\not{\epsilon}\not{k} - \not{k}\not{\epsilon}) \\ &+ g^{(4)}\gamma^\nu(\not{k}\not{\epsilon} - \not{\epsilon}\not{k})\not{p} \\ &+ g^{(5)}\gamma^\nu(p\cdot k\not{\epsilon} - p\cdot\epsilon\not{k})]\Gamma_\pm,\end{aligned} \tag{38}$$

where

$$g^{(1)} = -2ig^a_{N^*p\gamma} + 3ig^c_{N^*p\gamma} + g^d_{N^*p\gamma}, \tag{39}$$

$$g^{(2)} = -2ig^a_{N^*p\gamma} - g^b_{N^*p\gamma} + 2ig^c_{N^*p\gamma} - 2g^d_{N^*p\gamma}, \tag{40}$$

$$g^{(3)} = -ig^a_{N^*p\gamma} + ig^c_{N^*p\gamma}, \tag{41}$$

$$g^{(4)} = -ig^a_{N^*p\gamma} + ig^c_{N^*p\gamma}, \tag{42}$$

$$g^{(5)} = -2ig^a_{N^*p\gamma} + ig^c_{N^*p\gamma} - g^d_{N^*p\gamma}. \tag{43}$$

The hadronic vertex reads [16]

$$\begin{aligned}\Gamma^{\mu(\pm)}_{K\Lambda N^*} &= \frac{g_{K\Lambda N^*}}{m^2_{N^*}}\Gamma_\mp i\epsilon^{\mu\nu\rho\sigma}p_{\Lambda\nu}\gamma_5\gamma_\rho q_\sigma \\ &= \frac{g_{K\Lambda N^*}}{m^2_{N^*}}\Gamma_\mp[(p_\Lambda\cdot q - \not{p}_\Lambda\not{q})\gamma^\mu + \not{p}_\Lambda q^\mu - \not{q}p^\mu_\Lambda],\end{aligned} \tag{44}$$

where the second line of Eq. (44) is obtained by using Eq. (37). Therefore, the scattering amplitude can be derived and decomposed to the M_i matrices,

$$\begin{aligned}\mathcal{M}^{3/2}_{\text{res}} &= \bar{u}_\Lambda\Gamma^{\mu(\pm)}_{K\Lambda N^*}P^{3/2}_{\mu\nu}\Gamma^{\nu(\pm)}_{N^*p\gamma}u_p \\ &= \bar{u}_\Lambda\gamma_5\{(p_\Lambda\cdot q - \not{p}_\Lambda\not{q})\gamma^\mu + \not{p}_\Lambda q^\mu - \not{q}p^\mu_\Lambda\}(\not{p} + \not{k}\mp m_{N^*})(3P_{\mu\nu} + \gamma^\rho\gamma^\sigma P_{\mu\rho}P_{\nu\sigma}) \\ &\quad\times\{G^{(1)}(\epsilon^\nu\not{k} - k^\nu\not{\epsilon})\not{p} + G^{(2)}(k^\nu p\cdot\epsilon - \epsilon^\nu p\cdot k) + G^{(3)}p^\nu(\not{\epsilon}\not{k} - \not{k}\not{\epsilon}) + G^{(4)}\gamma^\nu(\not{k}\not{\epsilon} - \not{\epsilon}\not{k})\not{p} \\ &\quad + G^{(5)}\gamma^\nu(p\cdot k\not{\epsilon} - p\cdot\epsilon\not{k})\}u_p.\end{aligned} \tag{45}$$

Note that in Eq. (45) we have defined

$$G^{(i)} = \frac{sg^{(i)}g_{K\Lambda N^*}}{3m^6_{N^*}(s - m^2_{N^*} + im_{N^*}\Gamma_{N^*})}, \tag{46}$$

where $g^{(i)}$ are given by Eqs. (39)–(43) for $i = 1,\ldots,5$ and a factor of $s/m^2_{N^*}$ has been included in order to regularize the propagator [20,39].

Note that the terms proportional to the $G^{(4)}$ and $G^{(5)}$ in Eq. (45) vanish because they contain γ^ν, whereas it is clear that

$$\begin{aligned}\Big[&-3g_{\mu\nu} + \gamma_\mu\gamma_\nu + \frac{1}{s}\{(\not{p} + \not{k})\gamma_\mu(p + k)_\nu \\ &+ (p + k)_\mu\gamma_\nu(\not{p} + \not{k})\}\Big]\gamma^\nu = 0.\end{aligned} \tag{47}$$

Therefore, the remaining terms are

$$\begin{aligned}\mathcal{M}^{3/2}_{\text{res}} &= \bar{u}_\Lambda\gamma_5(\not{p}_\Lambda q^\mu - \not{q}p^\mu_\Lambda)(\not{p} + \not{k}\mp m_{N^*}) \\ &\quad\times(3\text{P}_{\mu\nu} + \gamma^\rho\gamma^\sigma\text{P}_{\mu\rho}\text{P}_{\nu\sigma}) \\ &\quad\times\{G^{(1)}(\epsilon^\nu\not{k} - k^\nu\not{\epsilon})\not{p} + G^{(2)}(k^\nu p\cdot\epsilon - \epsilon^\nu p\cdot k) \\ &\quad + G^{(3)}p^\nu(\not{\epsilon}\not{k} - \not{k}\not{\epsilon})\}u_p.\end{aligned} \tag{48}$$

By decomposing Eq. (48) in terms of the matrices M_i, we obtain the amplitudes $A_1, \ldots, A_6$ given in Appendix B by Eqs. (B1)–(B6).

2. Spin 5/2 in Model 2

In the case of spin 5/2, Model 2 utilizes the propagator similar to the case of Model 1, i.e., Eq. (26). However, in this model, we replace the factor $\sqrt{s}$ in Eq. (26) with the resonance mass m_{N^*}. The electromagnetic vertex is also similar to Eq. (38), but in this case, it has two indices, i.e., it is multiplied with the photon momentum k^β,

$$\begin{aligned}\Gamma^{\alpha\beta(\pm)}_{N^*p\gamma} = &-\frac{i}{m^3_{N^*}}\{g^{(1)}(\epsilon^\alpha \not{k} - k^\alpha \not{\epsilon})\not{p} \\ &+ g^{(2)}(k^\alpha p\cdot\epsilon - \epsilon^\alpha p\cdot k) \\ &+ g^{(3)}p^\alpha(\not{\epsilon}\not{k} - \not{k}\not{\epsilon}) + g^{(4)}\gamma^\alpha(\not{k}\not{\epsilon} - \not{\epsilon}\not{k})\not{p} \\ &+ g^{(5)}\gamma^\alpha(p\cdot k\not{\epsilon} - p\cdot\epsilon\not{k})\}k^\beta\Gamma_\mp, \end{aligned} \tag{49}$$

whereas the hadronic vertex [see Eq. (44)] has also two indices, i.e., it is multiplied with the hyperon momentum p^ν_Λ,

$$\begin{aligned}\Gamma^{\mu\nu(\pm)}_{K\Lambda N^*} &= \frac{g_{K\Lambda N^*}}{m^3_{N^*}}\Gamma_\pm i\epsilon^{\mu\alpha\rho\sigma}p_{\Lambda\alpha}\gamma_5\gamma_\rho q_\sigma p^\nu_\Lambda \\ &= \frac{g_{K\Lambda N^*}}{m^3_{N^*}}\Gamma_\pm\{(p_\Lambda\cdot q - \not{p}_\Lambda\not{q})\gamma^\mu \\ &\quad + \not{p}_\Lambda q^\mu - \not{q}p^\mu_\Lambda\}p^\nu_\Lambda. \end{aligned} \tag{50}$$

As a consequence, the scattering amplitude reads

$$\begin{aligned}\mathcal{M}^{5/2}_{\rm res} &= \bar{u}_\Lambda\Gamma^{\mu\nu(\pm)}_{K\Lambda N^*}P^{5/2}_{\mu\nu\alpha\beta}\Gamma^{\alpha\beta(\pm)}_{N^*p\gamma}u_p \\ &= \bar{u}_\Lambda\gamma_5\{(p_\Lambda\cdot q - \not{p}_\Lambda\not{q})\gamma^\mu + \not{p}_\Lambda q^\mu - \not{q}p^\mu_\Lambda\}p^\nu_\Lambda \\ &\quad\times(\not{p} + \not{k} \pm m_{N^*})(5P_{\mu\alpha}P_{\nu\beta} + 5P_{\mu\beta}P_{\nu\alpha} \\ &\quad - 2P_{\mu\nu}P_{\alpha\beta} + P_{\mu\rho}\gamma^\rho\gamma^\sigma P_{\sigma\alpha}P_{\nu\beta} + P_{\nu\rho}\gamma^\rho\gamma^\sigma P_{\sigma\beta}P_{\mu\alpha} \\ &\quad + P_{\mu\rho}\gamma^\rho\gamma^\sigma P_{\sigma\beta}P_{\nu\alpha} + P_{\nu\rho}\gamma^\rho\gamma^\sigma P_{\sigma\alpha}P_{\nu\beta}) \\ &\quad\times\{G^{(1)}(\epsilon^\alpha\not{k} - k^\alpha\not{\epsilon})\not{p} + G^{(2)}(k^\alpha p\cdot\epsilon - \epsilon^\alpha p\cdot k) \\ &\quad + G^{(3)}p^\alpha(\not{\epsilon}\not{k} - \not{k}\not{\epsilon})\}k^\beta u_p, \end{aligned} \tag{51}$$

where

$$G^{(i)} = \frac{s^2 g^{(i)} g_{K\Lambda N^*}}{10 m^{10}_{N^*}(s - m^2_{N^*} + i m_{N^*}\Gamma_{N^*})} \tag{52}$$

and $g^{(i)}$ are given by Eqs. (39)–(41) for $i = 1, \ldots, 3$.

Similar to the case of spin 3/2 discussed above, a factor of $s^2/m^4_{N^*}$ has been included in Eq. (52) in order to regularize the propagator [20,39]. Note also that in Eq. (51) the terms proportional to $g^{(4)}$ and $g^{(5)}$, i.e., Eqs. (42) and (43), have been excluded because they vanish after contracting γ^α in these terms [see Eq. (49)] with the propagator as in the case of spin 3/2 above. Explicitly, we can prove this by calculating

$$\begin{aligned}P^{5/2}_{\mu\nu\alpha\beta}\gamma^\alpha \propto &(5P_{\mu\alpha}P_{\nu\beta} + 5P_{\mu\beta}P_{\nu\alpha} - 2P_{\mu\nu}P_{\alpha\beta} \\ &+ P_{\mu\rho}\gamma^\rho\gamma^\sigma P_{\sigma\alpha}P_{\nu\beta} + P_{\nu\rho}\gamma^\rho\gamma^\sigma P_{\sigma\beta}P_{\mu\alpha} \\ &+ P_{\mu\rho}\gamma^\rho\gamma^\sigma P_{\sigma\beta}P_{\nu\alpha} + P_{\nu\rho}\gamma^\rho\gamma^\sigma P_{\sigma\alpha}P_{\nu\beta})\gamma^\alpha \\ = &\,5P_{\mu\alpha}P_{\nu\beta}\gamma^\alpha + 5P_{\mu\beta}P_{\nu\alpha}\gamma^\alpha - 2P_{\mu\nu}P_{\alpha\beta}\gamma^\alpha \\ &- 3P_{\mu\rho}\gamma^\rho P_{\nu\beta} - 2P_{\nu\rho}\gamma^\rho P_{\mu\beta} + 2P_{\mu\nu}P_{\alpha\beta}\gamma^\alpha \\ &+ P_{\mu\rho}\gamma^\rho\gamma^\sigma P_{\alpha\beta}P_{\nu\sigma}\gamma^\alpha - 2P_{\mu\rho}\gamma^\rho P_{\nu\beta} \\ &- P_{\mu\rho}\gamma^\rho\gamma^\sigma P_{\nu\sigma}P_{\alpha\beta}\gamma^\alpha - 3P_{\nu\rho}\gamma^\rho P_{\mu\beta} \\ = &\,0, \end{aligned} \tag{53}$$

where we have reordered the indices and used the fact that

$$g^{\mu\nu}P_{\mu\alpha}P_{\nu\beta} = -P_{\alpha\beta}. \tag{54}$$

By decomposing Eq. (51) into the M_i matrices via Eq. (3), we obtain the amplitudes A_i given in Appendix B by Eqs. (B15)–(B20).

IV. ENERGY-DEPENDENT WIDTH OF THE NUCLEON RESONANCE

Since the unitarity of the scattering amplitude is violated in a single-channel calculation, a proper correction at tree level is required. For this purpose, we include energy-dependent width in the resonance propagator [40]

$$\Gamma(\boldsymbol{q}) = \Gamma_{N^*}\frac{\sqrt{s}}{m_{N^*}}\sum_i x_i\left(\frac{|\boldsymbol{q}_i|}{|\boldsymbol{q}^{N^*}_i|}\right)^{2l+1}\frac{D_l(|\boldsymbol{q}_i|)}{D_l(|\boldsymbol{q}^{N^*}_i|)}, \tag{55}$$

where the sum runs over the possible decay channels into a meson and a baryon with mass m_i and m_b, respectively, and a relative momentum angular l.

The Γ_{N^*} in Eq. (55) represents the total decay width, whereas x_i is the relative branching ratio of the resonance to the i channel given in Table II. The final state momenta are given by

$$|\boldsymbol{q}^{N^*}_i| = \left[\frac{(m^2_{N^*} - m^2_b + m^2_i)^2}{4m^2_{N^*}} - m^2_i\right]^{1/2}, \tag{56}$$

and

$$|\boldsymbol{q}_i| = \left[\frac{(s - m^2_b + m^2_i)^2}{4s} - m^2_i\right]^{1/2}, \tag{57}$$

while the fission barrier function $D_l(\boldsymbol{q})$ reads [6]

$$D_l(\boldsymbol{q}) = \exp\left(-\frac{\boldsymbol{q}^2}{3\alpha^2}\right), \tag{58}$$

TABLE II. Relative branching ratios (x_i) used in Eq. (55) for the resonances used in the model. Values are taken or estimated from the PDG and references therein [7].

Resonance	πN	$\pi\pi N$	ηN	$K\Lambda$	$K\Sigma$
$N(1440)P_{11}$	0.65	0.35	0.00	0.00	0.00
$N(1520)D_{13}$	0.65	0.35	0.00	0.00	0.00
$N(1535)S_{11}$	0.50	0.05	0.45	0.00	0.00
$N(1650)S_{11}$	0.68	0.15	0.10	0.07	0.00
$N(1675)D_{15}$	0.40	0.59	0.00	0.01	0.00
$N(1680)F_{15}$	0.65	0.35	0.00	0.00	0.00
$N(1700)D_{13}$	0.10	0.87	0.00	0.03	0.00
$N(1710)P_{11}$	0.10	0.55	0.20	0.15	0.00
$N(1720)P_{13}$	0.11	0.77	0.04	0.08	0.00
$N(1860)F_{15}$	0.20	0.80	0.00	0.00	0.00
$N(1875)D_{13}$	0.12	0.84	0.04	0.00	0.00
$N(1880)P_{11}$[a]	0.30	0.30	0.30	0.05	0.05
$N(1895)S_{11}$[a]	0.30	0.30	0.30	0.05	0.05
$N(1900)P_{13}$[a]	0.30	0.30	0.30	0.05	0.05
$N(2000)F_{15}$[a]	0.30	0.30	0.30	0.05	0.05
$N(2060)D_{15}$[a]	0.30	0.30	0.30	0.05	0.05
$N(2120)D_{13}$[a]	0.30	0.30	0.30	0.05	0.05

[a]Only estimated. The value is not available in the PDG listing.

which is independent of l [6], with $\alpha = 410$ MeV. Since for a number of resonances the branching ratios are not known, we need to estimate their numerical values as shown in Table II. Note that this energy-dependent width prescription has been used in our previous studies [3,29–36].

V. RESULTS AND DISCUSSION

A. General results

We have included all the latest $K^+\Lambda$ photoproduction data in our fitting database. They consist of a differential cross section [41–45], recoil polarization [41,46], photon Σ and target T asymmetries [46], beam-recoil double polarization C_x and C_z [47], as well as $O_{x'}$ and $O_{z'}$ [48] data. We do not use the SAPHIR data [49] because they do not agree with other data used in this analysis. Including the SAPHIR data in the fitting database would result in a model which is inconsistent to all data sets [29]. For the sake of comparison between model calculations and experimental data near the threshold (Sec. V B), we will, however, show the SAPHIR data, because at this kinematics, the SAPHIR data are still consistent with other data.

In total, our fitting database consists of almost 7500 data points, i.e., two times larger than that used in our latest analysis [31]. So far, this is the largest $K^+\Lambda$ photoproduction database used to fit a single-channel isobar model.

TABLE III. Four combinations of the spin-3/2 and −5/2 formulations used in the isobar model of the present analysis.

Model	Spin 3/2	Spin 5/2
Model A	Model 1	Model 1
Model B	Model 2	Model 1
Model C	Model 1	Model 2
Model D	Model 2	Model 2

The possible combinations of using Model 1 and Model 2 formulations in the spin-3/2 and spin-5/2 nucleon resonance amplitudes of our isobar model are summarized in Table III. As a consequence, we have four different combinations, which are referred to as models A, B, C, and D. The number of fitted resonance coupling constants is between 28 (Model A) and 50 (Model D). In addition to that, we also fit 12 background parameters as shown in Table IV. The leading coupling constants $g_{K\Lambda N}$ and $g_{K\Sigma N}$ are limited to the SU(3) values with 20% symmetry breaking [50], i.e., $g_{K\Lambda N}/\sqrt{4\pi} = -4.40 \cdots -3.00$ and $g_{K\Sigma N}/\sqrt{4\pi} = +0.90 \cdots +1.30$. We also allow the mass and width of resonances to vary within the PDG error bars

TABLE IV. Extracted background parameters and the resonance hadronic cutoff Λ_R from the fit to experimental data for all models considered in the present analysis. See our previous works [3,29–36] for the notation of the parameters. The number of fitted parameters is given by $N_{\rm par}$, whereas the number of used data is $N = 7433$.

Parameters	A	B	C	D
$g_{K\Lambda N}/\sqrt{4\pi}$	−3.37	−3.00	−3.00	−3.00
$g_{K\Sigma N}/\sqrt{4\pi}$	0.90	0.90	1.30	1.27
$G^V_{K^*}/4\pi$	−0.25	0.12	−0.37	0.15
$G^T_{K^*}/4\pi$	0.17	−0.08	0.72	0.26
$G^V_{K_1}/4\pi$	0.42	0.43	0.23	1.46
$G^T_{K_1}/4\pi$	−0.72	−0.08	−0.91	0.07
$G_{\Lambda(1600)}/4\pi$	−6.30	−9.00	5.12	8.41
$G_{\Lambda(1810)}/4\pi$	10.00	10.00	−4.48	−9.61
Λ_B (GeV)	0.72	0.89	0.70	0.70
Λ_R (GeV)	2.00	2.0	2.00	1.31
$\theta_{\rm had}$ (deg)	180	122	56	130
$\phi_{\rm had}$ (deg)	72	180	180	177
χ^2	15736	13192	14679	11724
$N_{\rm par}$	74	86	84	96
χ^2/N	2.14	1.77	1.97	1.58

[7]. The minimization process is performed by using the CERN-MINUIT code.

The extracted background parameters for all models (A–D) are shown in Table IV. It is apparent that, except in Model B, the background hadronic cutoff Λ_B tends to be small (soft form factor), whereas the leading coupling constants in all models tend to reach their lower bounds. Therefore, in most cases, there is a tendency that the background terms are suppressed, whereas the resonance terms are not, which is indicated by the relatively large cutoff (hard form factor) in the latter. The same finding has been obtained in our previous works [3,29,31,32], although in Ref. [32], we have shown that we could slightly soften the hadronic cutoff by using the $\Lambda(1600)P_{01}$ and $\Lambda(1810)P_{01}$ hyperon resonances. The different result obtained in the present work can be understood as the consequence of using a large number of data, which is clearly stretching the limit of validity of the model to high energies. To this end, a small background contribution is inevitably required.

The values of total χ^2 as well as χ^2/N given in the lower part of Table IV are as expected; i.e., the largest (smallest) χ^2 is obtained in the model using the smallest (largest) number of free parameters. Nevertheless, the improvement obtained after using the vertex and propagator formula of Model 2 for both spins 3/2 and 5/2 is quite significant. As discussed later, the agreement of model calculation and experimental data is excellent for Model D. Note that by looking at the values of χ^2/N given in the lower part of Table IV and the spin model combinations in Table III we may suspect that the spin-3/2 formalism of Model 1 could become the origin of the large χ^2 value or the difficulty to nicely reproduce the data [51], since the χ^2 value does not significantly decrease if the spin-3/2 formalism of Model 1 is used (Model A and Model C). We will come back to this problem later when we discuss the calculated cross section near threshold in the next subsection.

The extracted resonance coupling constants are listed in Table V. In this case, comparison between coupling constants of different models is difficult, except for the spin-1/2 resonances, since all models use the same spin-1/2 formulation. For completeness, we also display the extracted masses and widths of nucleon resonances, where the values have been varied within the error bars of the PDG values [7].

The total cross sections obtained in the present work compared with the prediction of Kaon–Maid [3] as well as the experimental data from CLAS [41] are shown in Fig. 3. Obviously, Kaon–Maid cannot explain the data for $W \geq 1.7$ GeV. The reason has been discussed in detail in Ref. [29]. Interestingly, Model A exhibits an oscillation around the experimental data from threshold up to $W = 2$ GeV. Note that Model A utilizes the propagator

TABLE V. Extracted resonance coupling constants from the fit to experimental data for all models considered in the present analysis.

Coupling	A	B	C	D
$G_{N(1440)}/4\pi$	−0.44	0.85	−0.31	1.52
$G^{(1)}_{N(1520)}/4\pi$	0.07	−0.05	0.06	−0.00
$G^{(2)}_{N(1520)}/4\pi$	0.06	−0.63	0.11	0.68
$G^{(3)}_{N(1520)}/4\pi$	⋯	−0.08	⋯	0.07
$G^{(4)}_{N(1520)}/4\pi$	⋯	0.26	⋯	−0.32
$G_{N(1535)}/4\pi$	−0.24	−0.04	0.28	−0.15
$G_{N(1650)}/4\pi$	0.76	0.16	0.21	−0.04
$G^{(1)}_{N(1675)}/4\pi$	2.07	−0.12	−0.67	0.01
$G^{(2)}_{N(1675)}/4\pi$	0.68	1.09	−1.99	0.87
$G^{(3)}_{N(1675)}/4\pi$	⋯	⋯	−0.73	0.07
$G^{(4)}_{N(1675)}/4\pi$	⋯	⋯	1.01	−0.01
$G^{(1)}_{N(1680)}/4\pi$	6.72	6.25	−0.80	2.74
$G^{(2)}_{N(1680)}/4\pi$	3.96	2.87	9.99	0.05
$G^{(3)}_{N(1680)}/4\pi$	⋯	⋯	−1.69	2.54
$G^{(4)}_{N(1680)}/4\pi$	⋯	⋯	−4.42	0.44
$G^{(1)}_{N(1700)}/4\pi$	0.14	−0.14	0.08	0.25
$G^{(2)}_{N(1700)}/4\pi$	0.05	−1.03	−0.02	0.62
$G^{(3)}_{N(1700)}/4\pi$	⋯	−0.34	⋯	0.51
$G^{(4)}_{N(1700)}/4\pi$	⋯	0.39	⋯	−0.20
$G_{N(1710)}/4\pi$	0.50	0.21	0.16	−0.41
$G^{(1)}_{N(1720)}/4\pi$	0.47	0.31	0.45	0.28
$G^{(2)}_{N(1720)}/4\pi$	0.78	−0.09	1.40	−0.36
$G^{(3)}_{N(1720)}/4\pi$	⋯	0.25	⋯	0.17
$G^{(4)}_{N(1720)}/4\pi$	⋯	0.06	⋯	−0.21
$G^{(1)}_{N(1860)}/4\pi$	−3.82	−6.60	3.06	−2.20
$G^{(2)}_{N(1860)}/4\pi$	−1.44	−4.37	−9.53	−9.99
$G^{(3)}_{N(1860)}/4\pi$	⋯	⋯	7.76	−2.28
$G^{(4)}_{N(1860)}/4\pi$	⋯	⋯	4.38	3.12
$G^{(1)}_{N(1875)}/4\pi$	0.05	0.17	0.03	−0.13
$G^{(2)}_{N(1875)}/4\pi$	0.04	1.50	0.02	−0.09

(Table continued)

TABLE V. (*Continued*)

Coupling	A	B	C	D
$G^{(3)}_{N(1875)}/4\pi$	⋯	0.46	⋯	−0.54
$G^{(4)}_{N(1875)}/4\pi$	⋯	−0.61	⋯	0.11
$G_{N(1880)}/4\pi$	−0.11	0.19	−0.08	0.33
$G_{N(1895)}/4\pi$	0.01	−0.01	0.03	0.01
$G^{(1)}_{N(1900)}/4\pi$	−0.18	−0.33	−0.09	0.02
$G^{(2)}_{N(1900)}/4\pi$	0.02	0.19	−0.23	−0.21
$G^{(3)}_{N(1900)}/4\pi$	⋯	−0.26	⋯	0.05
$G^{(4)}_{N(1900)}/4\pi$	⋯	−0.10	⋯	0.38
$G^{(1)}_{N(2000)}/4\pi$	−3.89	−4.47	−3.10	−1.44
$G^{(2)}_{N(2000)}/4\pi$	−2.68	−2.43	−9.99	9.75
$G^{(3)}_{N(2000)}/4\pi$	⋯	⋯	−7.51	0.33
$G^{(4)}_{N(2000)}/4\pi$	⋯	⋯	4.31	−4.13
$G^{(1)}_{N(2060)}/4\pi$	−1.27	0.02	1.07	−0.69
$G^{(2)}_{N(2060)}/4\pi$	2.83	−1.83	3.32	0.82
$G^{(3)}_{N(2060)}/4\pi$	⋯	⋯	1.24	−0.91
$G^{(4)}_{N(2060)}/4\pi$	⋯	⋯	−1.71	−1.51
$G^{(1)}_{N(2120)}/4\pi$	0.01	−0.03	0.02	0.05
$G^{(2)}_{N(2120)}/4\pi$	0.03	1.53	0.07	1.40
$G^{(3)}_{N(2120)}/4\pi$	⋯	−0.02	⋯	0.06
$G^{(4)}_{N(2120)}/4\pi$	⋯	−0.60	⋯	−0.57

and vertex factors that are commonly used in the analysis of kaon photo- or electroproduction [13]. We have also observed the difficulty to obtain small χ^2 by using this model. The origin of the oscillation in the total cross section shown in Fig. 3 will be discussed in detail in Sec. V B, when we discuss the production near threshold.

From Fig. 3, we might suspect that the agreement of the best model (Model D) with experimental data seems to be valid only up to $W \approx 2.3$ GeV. Above this energy, the calculated cross section starts to underpredict the data. This happens because, compared to the older CLAS data [41] (from now on called CLAS 2006), the more recent ones [42] (from now on called CLAS 2010) have a smaller differential cross section at forward angles. A small fraction of these data is shown in the bottom panel of Fig. 4. Clearly, the best fit will be only achieved by lowering the cross section at this kinematics, especially because the CLAS 2010 data [42] have smaller error bars (see the bottom panel of Fig. 4). It is also important to note that the situation is quite different in the low-energy region, i.e., near the threshold, where the CLAS 2010 data overshoot the CLAS 2006 data.

The differential cross section at the very forward angle shown in the bottom panel of Fig. 4 reveals the current problem in the analysis of both hyperon and hypernuclear photoproductions. Because of the high momentum transfer, the cross section of the hypernuclear photoproduction is sizable only at the forward kinematics. Therefore, an accurate information of the elementary photoproduction of kaon-hyperon on the proton is urgently required, since the effect on the hypernuclear prediction is substantial. However, as can be seen in the bottom panel of Fig. 4, the currently available data are significantly scattered and, as a consequence, produce a large uncertainty in the forward angle. The best model is only able to reproduce the average values of the cross section, in order to minimize the χ^2. Thus, future experimental proposals should be focused on this problem before considering the high-energy regions.

Near the threshold, there seems to be a problem, since the CLAS 2010 and Crystal Ball [45] data show a sharp peak at $W \approx 1650$ MeV. All models fail to reproduce this

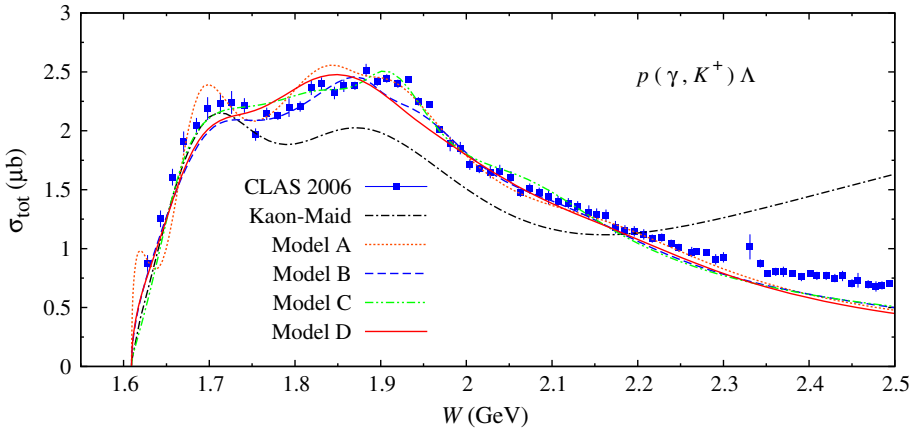

FIG. 3 (color online). Calculated total cross sections obtained from Kaon–Maid [3], models A, B, C, and D, compared with the experimental data from the CLAS Collaboration [41]. Note that the experimental data shown in this figure are not included in the fitting database.

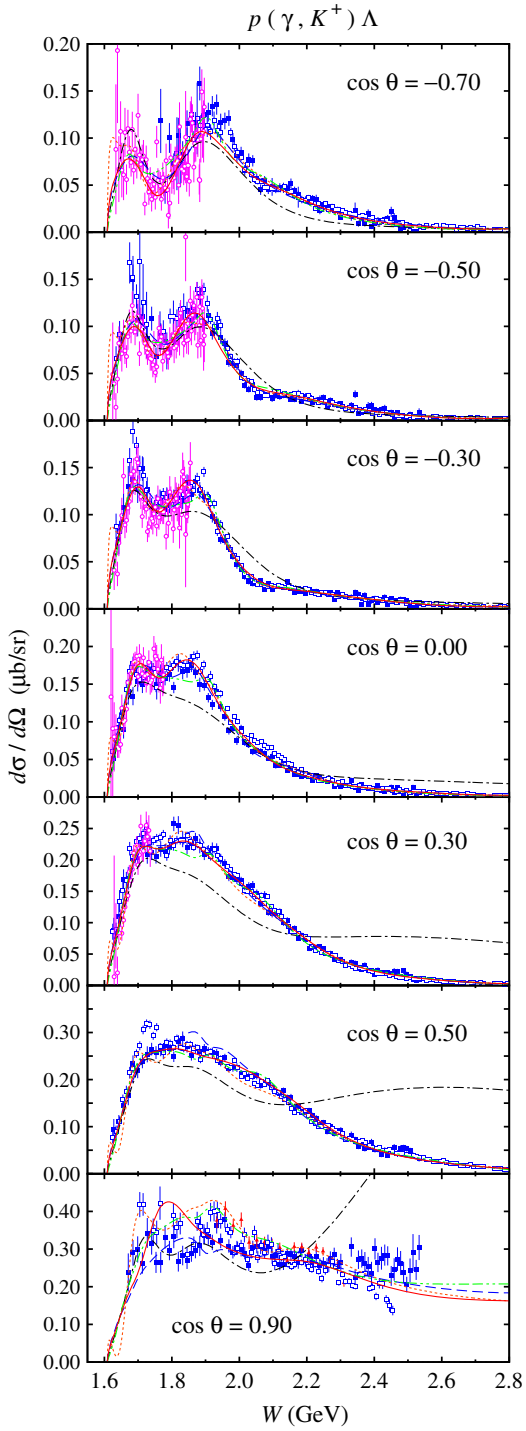

FIG. 4 (color online). Differential cross sections for the $\gamma + p \to K^+ + \Lambda$ channel as a function of the total c.m. energy W for different values of the kaon c.m. angle. Experimental data are from the CLAS Collaboration (solid squares [41] and open squares [42]), LEPS Collaboration (solid triangles [43]), and Crystal Ball Collaboration (open circles [45]). Notation of the curves is as in Fig. 3.

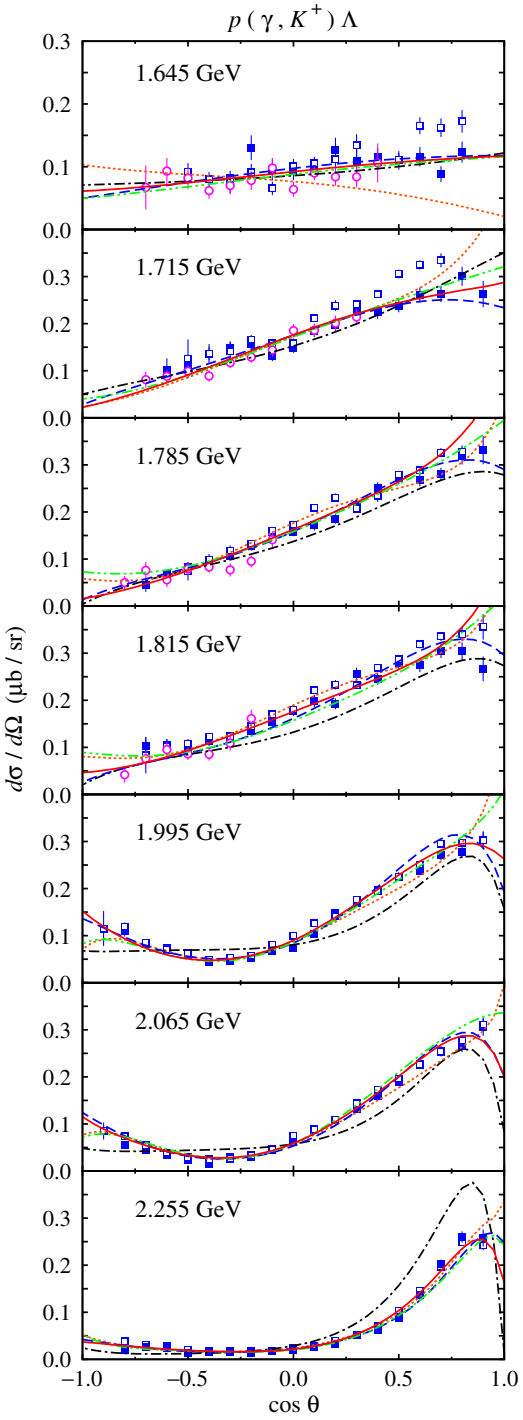

FIG. 5 (color online). As in Fig. 4, but for the angular distribution of differential cross section with different values of the total c.m. energy W.

peak. Nevertheless, since the present analysis is focused on the different effects of the spin-3/2 and −5/2 models, we do not worry too much about this problem. Furthermore, the CLAS 2006 data do not show this phenomenon, the peak only appears at the backward direction, and the data error bars at this kinematics are significantly large. In the previous analysis [4,5], it was shown that this peak can be nicely explained by including a special resonance with a very narrow width in the model. This very resonance belongs to the nonstrange member of the antidecuplet baryons predicted by the chiral quark soliton model [52].

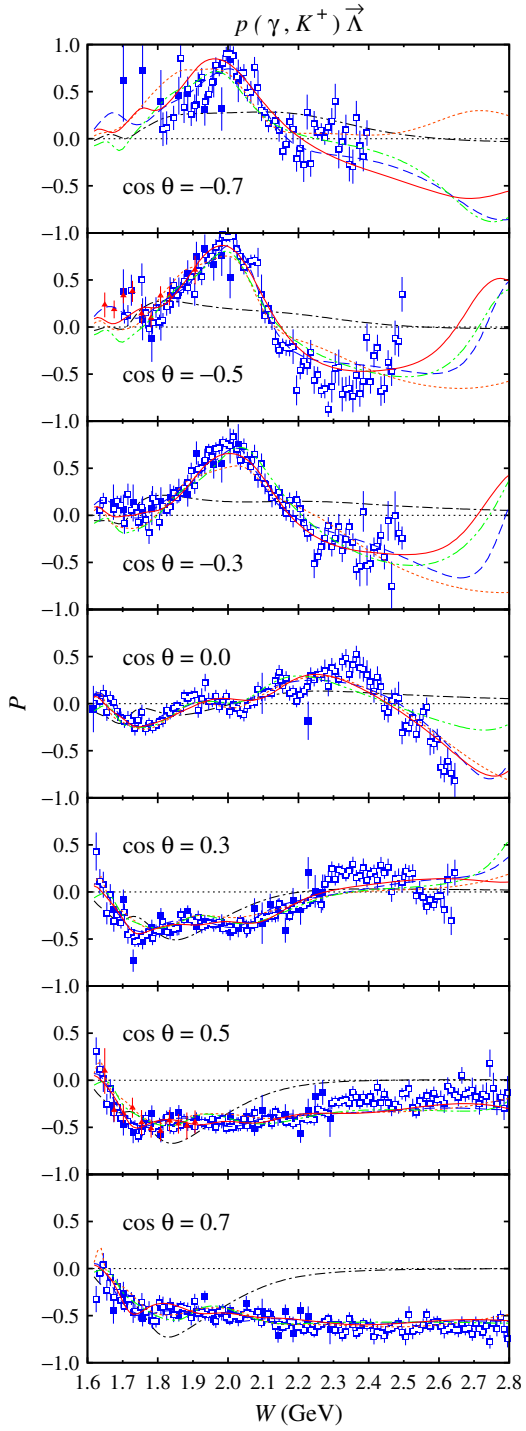

FIG. 6 (color online). Λ recoil polarization as a function of the total c.m. energy W for different values of the kaon c.m. angle. Notation of the curves and experimental data is as in Fig. 4.

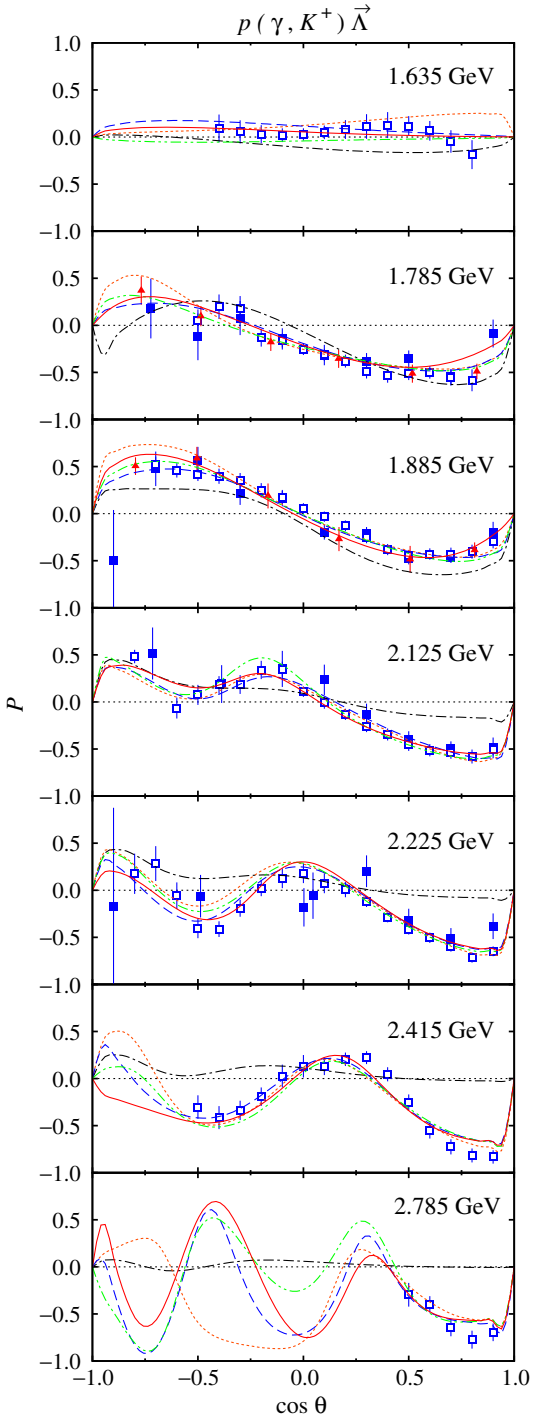

FIG. 7 (color online). As in Fig. 6, but for the angular distribution of the Λ recoil polarization with different values of the total c.m. energy W.

We refer the reader to Refs. [4,5] for a thorough discussion on this subject.

The deficiency of Model A is clearly elucidated in the top panel of Fig. 5, where at low energy Model A yields a backward peaking differential cross section, in contrast to the experimental data and other models. The difficulty to obtain a small χ^2 can be understood from Fig. 5, where the discrepancy between the CLAS 2006 and CLAS 2010 cross section data clearly appears for $W \lesssim 1.9$ GeV and only by reproducing the average values of these cross sections could the lowest χ^2 be obtained. In general, however, Model D displays the

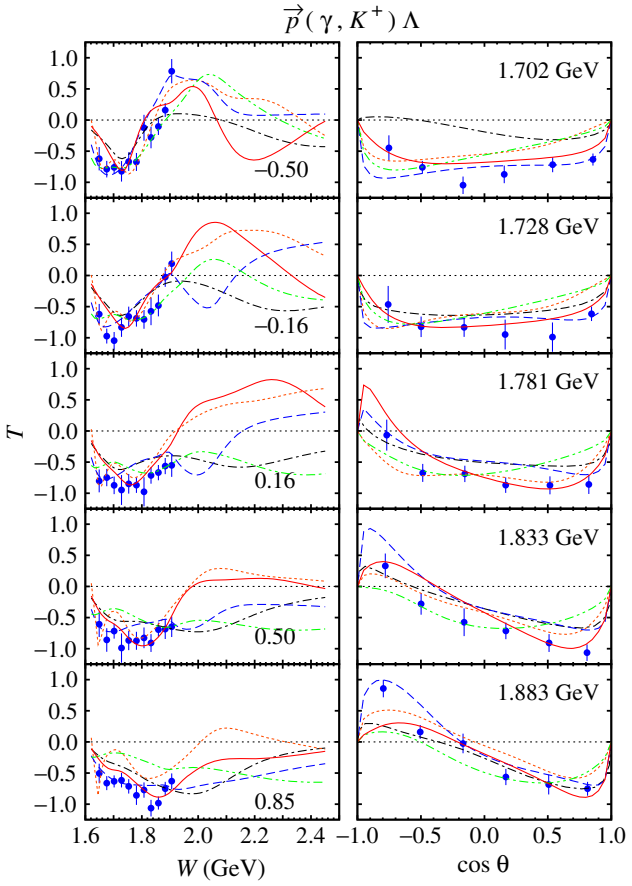

FIG. 8 (color online). Target asymmetry as functions of the total c.m. energy and kaon angles. Notation of the curves is as in Fig. 3. Experimental data are from the GRAAL Collaboration [46].

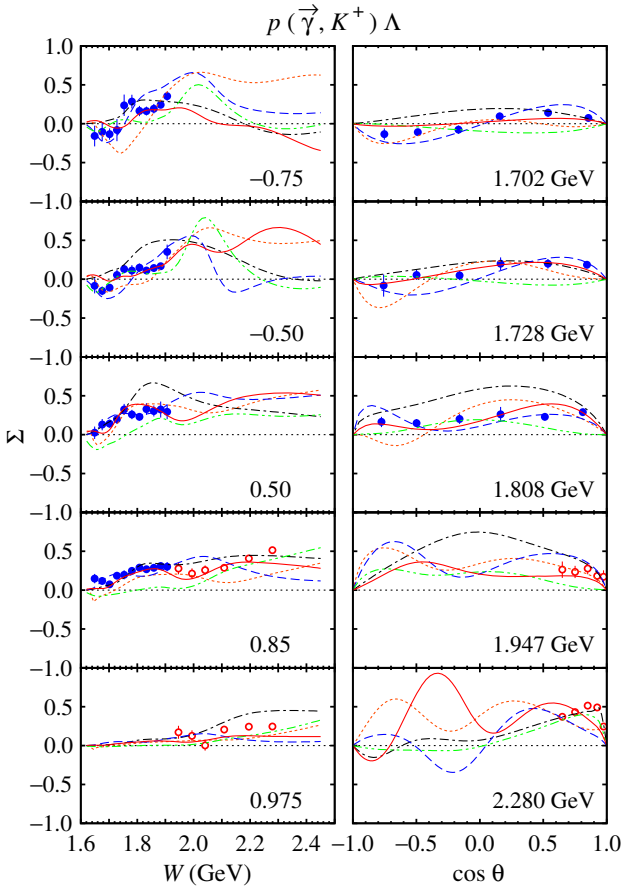

FIG. 9 (color online). Photon asymmetry as functions of the total c.m. energy and kaon angles. Notation of the curves is as in Fig. 3. Experimental data are from the LEPS [43] (open circles) and GRAAL [46] (closed circles) collaborations.

best agreement with experimental data, as compared to other models.

To our knowledge, reproducing the recoil polarization observable accurately is extremely difficult. This is because the recoil polarization depends sensitively on the ingredient of the scattering amplitude $\mathcal{M}$. Therefore, the recoil polarization data could provide a tough constraint on the theoretical or phenomenological explanations of the kaon photoproduction. Furthermore, the recoil polarization could also reveal the phenomena that do not show up in the differential cross section, e.g., the indication of the 1650 MeV narrow nucleon resonance [4].

The calculated recoil polarization obtained from Models A, B, C, and D are displayed in Figs. 6 and 7. It is obvious from the two figures that Model D produces the best agreement with experimental data. At high energies ($W \gtrsim 2.0$ GeV) and backward direction, the discrepancy between models starts to become significant. Unfortunately, the accuracy of the experimental data is the worst at this kinematics, although some interesting structures are indicated by the data at 2.0 Ge V $\lesssim W \lesssim 2.5$ GeV.

The target and photon asymmetries shown in Figs. 8 and 9, respectively, could also become the important constraints to select the best model for kaon photoproduction, since the asymmetries calculated from the four models show a large variance. In the case of target asymmetry, it is found that no model can perfectly reproduce the whole data shown in Fig. 8. Presumably, this is due to the number of experimental data for the target asymmetry, which is very small as compared to that of the differential cross section as well as the recoil polarization data. Moreover, the average error bars of the target asymmetry are relatively large. Actually, this problem could be solved by introducing a weighting factor for this observable in the fitting process. However, we believe that this is not urgent since in the present analysis only comparison between the models is required.

In contrast to the target asymmetry, experimental data for the photon asymmetry shown in Fig. 9 can be nicely reproduced by Model D, whereas other models show significant disagreement with experimental data, especially with the LEPS data. This fact is interesting, because in the case of the target asymmetry, the number of data is also

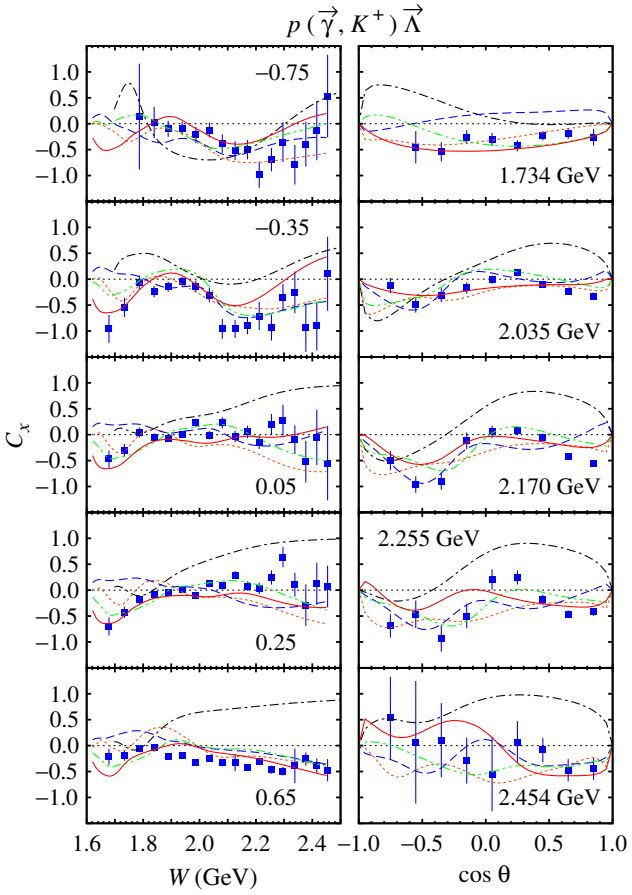

FIG. 10 (color online). As in Fig. 9, but for the beam-recoil double polarization observable C_x. Experimental data are from the CLAS Collaboration [47].

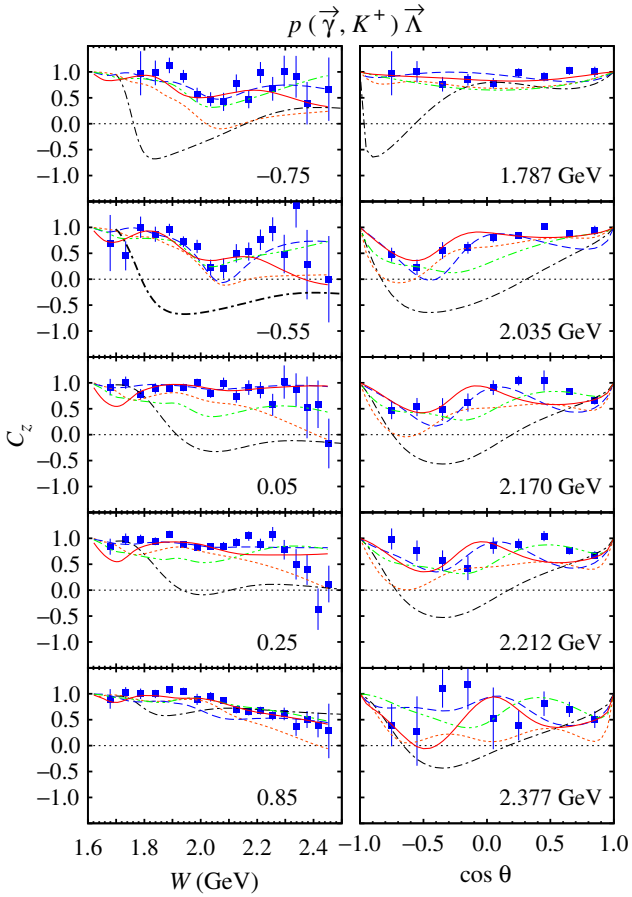

FIG. 11 (color online). As in Fig. 9, but for the beam-recoil double polarization observable C_z. Experimental data are from the CLAS Collaboration [47].

small, but the agreement with Model D is only fair. The relatively smaller error bars in the photon asymmetry case could become the reason behind this phenomenon.

The double polarization observables C_x, C_z, $O_{x'}$, and $O_{z'}$ displayed in Figs. 10, 11, 12, and 13, respectively, are interesting observables because they indicate that the Λ hyperons are produced with 100% polarization as seen by combining C_x, C_z, and the induced polarization P via $R \equiv \sqrt{C_x^2 + C_y^2 + P^2} = 1.01 \pm 0.01$ [53]. In the case of $O_{x'}$ and $O_{z'}$, the relation $R \equiv \sqrt{O_{x'}^2 + O_{y'}^2 + P^2} \approx 1$ is only partially fulfilled [48]. Figures 10–13 show that Model D can nicely explain these observables, in contrast to other models.

B. Kaon photoproduction near threshold

Meson photoproduction near threshold plays an important role in the investigation of the low-energy theorem, chiral perturbation theory, as well as quark models [54]. In the case of kaon photoproduction, the main advantage is, however, slightly different, i.e., reducing the number of participating resonances in the model. As it is well known in kaon production, the number of contributing resonances at the energies, where most of the experimental data are available, is quite large. Therefore, limiting the number of resonances is clearly desired, because the number of uncertainties in the model is proportional to the number of resonances. For instance, by limiting the energy of interest up to 50 MeV above the $K^+\Lambda$ photoproduction threshold, only the $N(1650)S_{11}$ resonance state can contribute to the process [30].

There have been a number of investigations devoted to the kaon photoproduction near the threshold energy in the literature [30,36,55–57]. The results of previous studies based on multipoles analysis [30] and chiral perturbation theory [55] compared with that obtained in the present analysis are shown in Fig. 14, where we have limited the energy only up to 1.75 GeV, i.e., about 140 MeV above the threshold. As discussed in our previous work [30], the prediction of chiral perturbation theory underestimates the data, whereas the result of the multipoles model with pseudoscalar coupling is in good agreement with the experimental data. From Fig. 14, it is apparent that, except

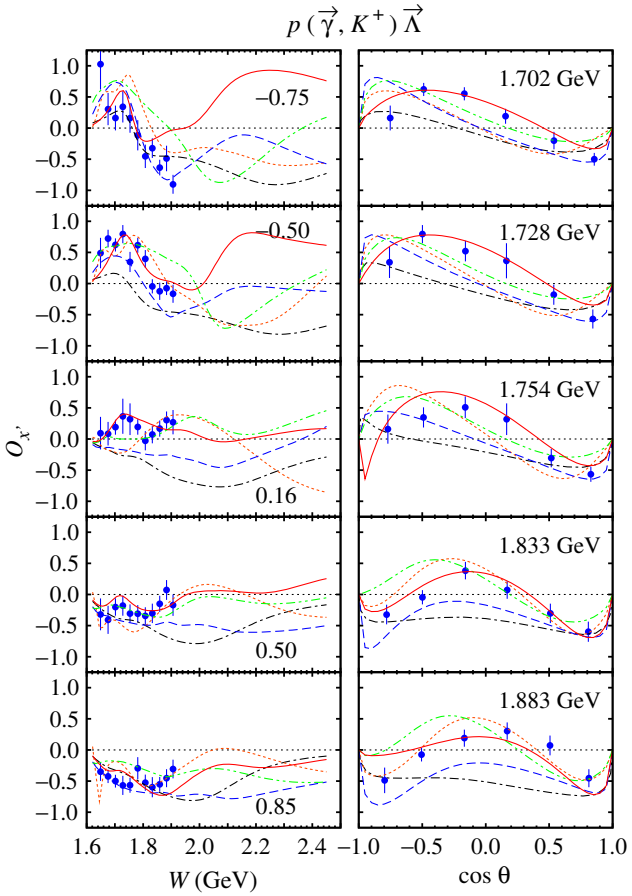

FIG. 12 (color online). As in Fig. 9, but for the beam-recoil double polarization observable O_x. Experimental data are from the GRAAL Collaboration [48].

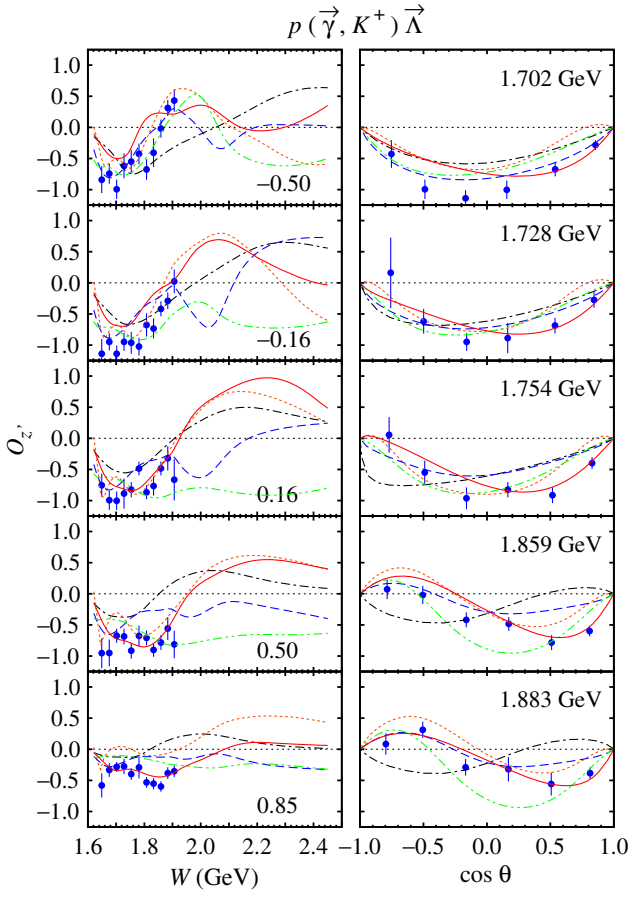

FIG. 13 (color online). As in Fig. 12, but for the beam-recoil double polarization observable O_z. Experimental data are from the GRAAL Collaboration [48].

for Model A, all models in the present analysis can nicely reproduce the total cross section data within their error bars. However, in spite of having the smallest χ^2, the best model (Model D) seems to slightly underpredict the CLAS total cross section data. As in the case of higher energies discussed in the previous subsection, we can understand this phenomenon as the effect of other differential cross section data used in the fit, i.e., the Crystal Ball data [45] (open circles in Fig. 15).

The oscillating cross section that is obtained from Model A and shown previously in Fig. 3 can be clearly seen in Fig. 14. We have investigated this oscillation and found that it originates from the extra large contributions of the $N(1650)S_{11}$ and $N(1700)D_{13}$ resonances. As shown in the second column of Table V, the coupling constant of the $N(1650)S_{11}$ is much larger than those of the other S_{11} resonances, i.e., the $N(1535)S_{11}$ and $N(1895)S_{11}$. This is also obvious if we compare it with the corresponding coupling constant in other models, except in Model C. By comparing the coupling constants of the $N(1700)D_{13}$ resonance with those of the $N(1520)D_{13}$, $N(1875)D_{13}$, and $N(2120)D_{13}$ resonances in model A (second column of Table V), we observe also the same pattern. Note that comparing the coupling constants of the $N(1700)D_{13}$ resonance in Model A with those in other models is complicated since in the latter the formulation of spin 3/2 is different, except in Model C. In Model C, we can

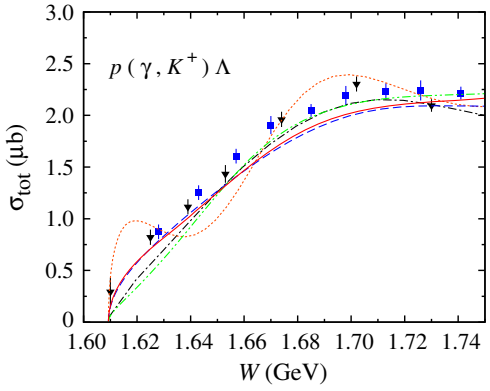

FIG. 14 (color online). Total cross section as in Fig. 3, but limited to the threshold region. The multipoles model is taken from Ref. [30], whereas the result of chiral perturbation theory (χPT) is obtained from Ref. [55]. The solid inverted triangles display the SAPHIR data [49]. All data shown in this figure were not included in our fitting database.

see that the coupling constants of the $N(1650)S_{11}$ and $N(1700)D_{13}$ resonances are comparable to those of Model A. This fact explains the existence of a small oscillation in the cross section of Model C, as depicted in Fig. 14.

We note that a large contribution of the $N(1650)S_{11}$ resonance near the kaon production threshold is natural and was found in our previous investigations [4,30]. However, we found that in Model A the $N(1650)S_{11}$ contribution alone yields a total cross section an order of magnitude larger than the experimental data at $W = 1650$ MeV. The same result is also obtained by using the $N(1700)D_{13}$ resonance alone. In contrast to this, in our previous investigations, we obtained that this resonance yields a smaller cross section compared to the experimental data at $W = 1650$ MeV (see Fig. 2 of Ref. [30] and Fig. 2 of Ref. [4]).

To reproduce the experimental data, a destructive interference between the $N(1650)S_{11}$ and $N(1700)D_{13}$ contributions is inevitable. However, the result of this interference cannot be easily smoothed by a complicated interference with contributions from the other resonances. Therefore, an oscillating cross section could be the best solution for reproducing the experimental data, in which the large error bars of the new Crystal Ball data fortunately allow for an oscillation of the differential cross section as shown in Fig. 15. As noted in Ref. [45], the new Crystal Ball data are consistent with the SAPHIR data [49], and this is surprisingly proven in the bottom panel of Fig. 15, although the SAPHIR data [49] were not used in the fitting process. It is also important to mention at this stage that our previous multipole analysis [29] indicates that both $N(1650)S_{11}$ and $N(1700)D_{13}$ resonances are more (and very) important in the case of fitting to the SAPHIR data rather than to the CLAS data (see Fig. 2 of Ref. [29]).

Figure 16 emphasizes the result shown previously in Fig. 5, i.e., the wrong backward peaking differential cross section obtained by Model A. Indeed, this problem appears up to $W \approx 1.66$ GeV. Interestingly, such behavior is not shown by Model C, that also exhibits the oscillating cross section, although milder than Model A. The effect of the spin-5/2 formalism of Model 2 could be the origin of this phenomenon.

The above results and the χ^2 obtained by Model A and Model C given in Table IV indicate that the formalism of spin 3/2 in Model 1 leads to a problem in reproducing the experimental data. To some extent, replacing the spin-3/2 formalism with that of Model 2 improves substantially the model. Nevertheless, the best result would be obtained by using Model 2 in the formalisms of both spins 3/2 and 5/2.

VI. COMPARISON WITH OTHER MODELS

Although the main purpose of this paper is to compare the effects of different formulations of spin-3/2 and spin-5/2 nucleon resonances in kaon photoproduction, comparison of the best model obtained in the present work, i.e., Model D, with other existing models is of course of interest.

The extracted nucleon resonance masses and widths can be compared with the Breit–Wigner ones estimated

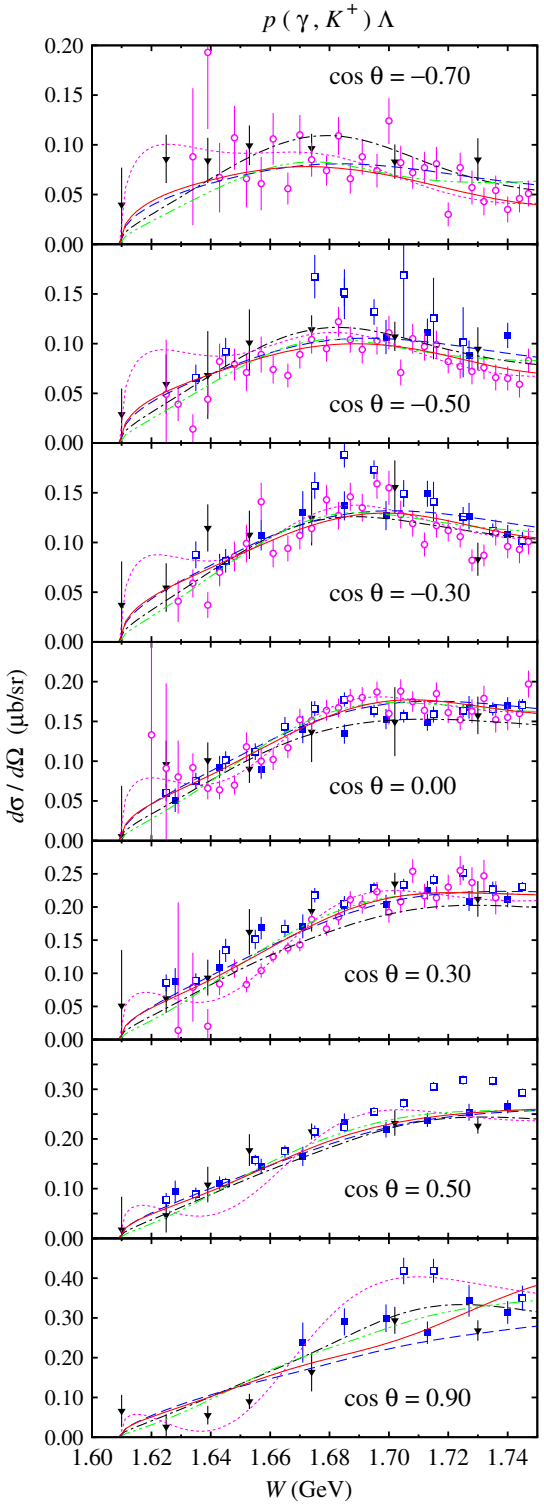

FIG. 15 (color online). As in Fig. 4, but limited to the threshold region. The solid inverted triangles display the SAPHIR data [49], which were not used in the fitting process.

by the PDG [7] as well as those obtained by the Giessen [58] and Bonn–Gatchina [59] models. The comparison is shown in Figs. 17 and 18. The extracted masses and widths are clearly consistent with the PDG estimate since during the fit process we only allow the variation of the masses and widths within the PDG error bars [7]. The small mass and width uncertainties obtained in the present work, as shown in Figs. 17 and 18, indicates that the fit is sensitive to the variation of the masses and widths of the nucleon resonances. There are no special trends or patterns shown by the extracted masses and widths, except we observe that for higher nucleon resonance mass the fit tends to prefer the upper values of the masses (see Fig. 17). Contrary to this, the extracted widths mostly tend to choose their lower limits.

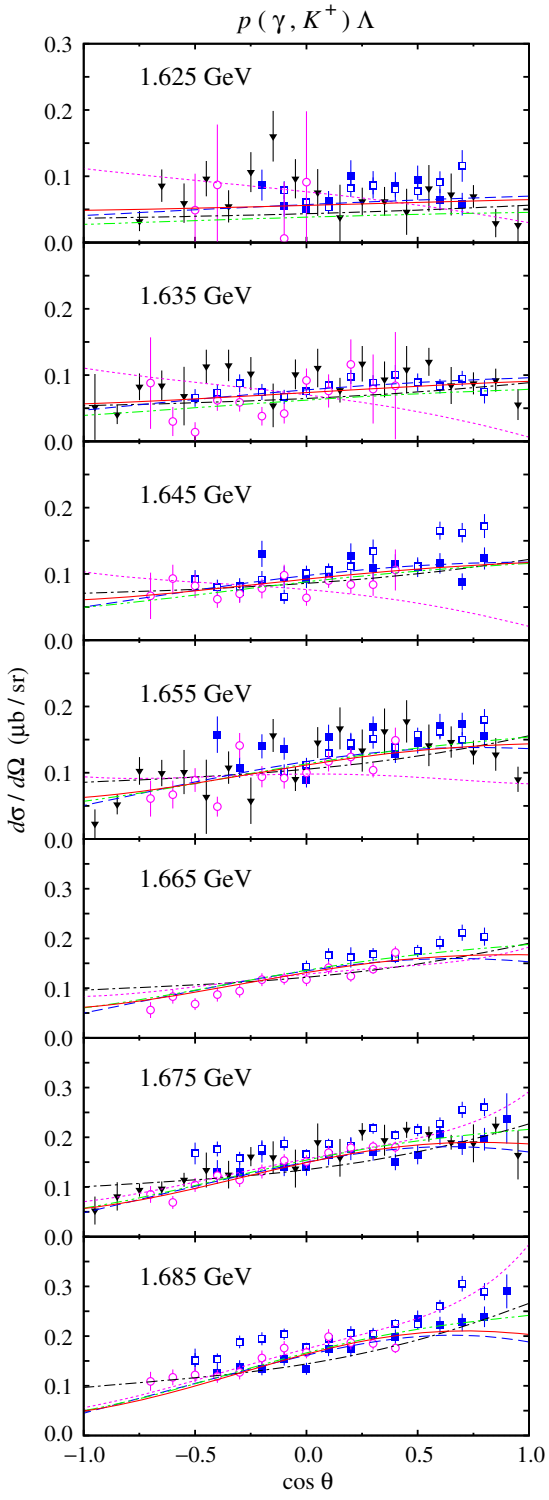

FIG. 16 (color online). As in Fig. 5, but limited to the threshold region. The solid inverted triangles display the SAPHIR data [49], which were not used in the fitting process.

Comparison between the calculated observables obtained from different models is shown in Figs. 19–24. For this purpose, we compare the calculated observables obtained from Model D with those from the Bonn–Gatchina model [59] and the Argonne National Laboratory (ANL)-Osaka dynamical coupled-channel model [1]. Note that we choose the same kinematics as that given in the ANL-Osaka paper [1], because the web version of this model is not available. The case of the differential cross section is shown in Fig. 19, where we can see that the agreement of our best model (Model D) with experimental data is excellent. In fact, it is comparable with the result from the Bonn–Gatchina partial wave analysis [59], although the number of the nucleon and hyperon resonances used in the present analysis is much smaller. Especially remarkable is in the forward directions for medium and high energies, where we see that the ANL-Osaka dynamical coupled-channel analysis show significant deficiencies. The present analysis seems to underpredict the experimental data only for $1.665 \lesssim W \lesssim 1.705$ GeV in the forward direction. However, as previously shown in Fig. 16, the old [41] and new [42] CLAS data show a relatively significant discrepancy at this kinematics. Figure 16 also exhibits that the SAPHIR data are consistent with the present analysis, although they are not included in the fitting database. Note that the problem of inconsistency between the CLAS [41] and SAPHIR [49] data appears at $W \gtrsim 1.7$ GeV [29].

For the recoiled Λ polarization displayed in Fig. 20, our best model can nicely reproduce the experimental data. Except for $W = 1.625$ GeV, where theoretically the polarization should be small and no model can explain the existing data, the calculated polarization obtained from Model D has the best agreement with experimental data. In the higher energy regions, all three models tend to converge, except for very few and certain kinematics. A reliable description of this polarization is demanded, because it has been shown that there is an indication of the narrow resonance which originates from this polarization at $W = 1.650$ GeV [4,5].

In the case of photon asymmetry given in Fig. 21, we can see that all models can in principle reproduce the data.

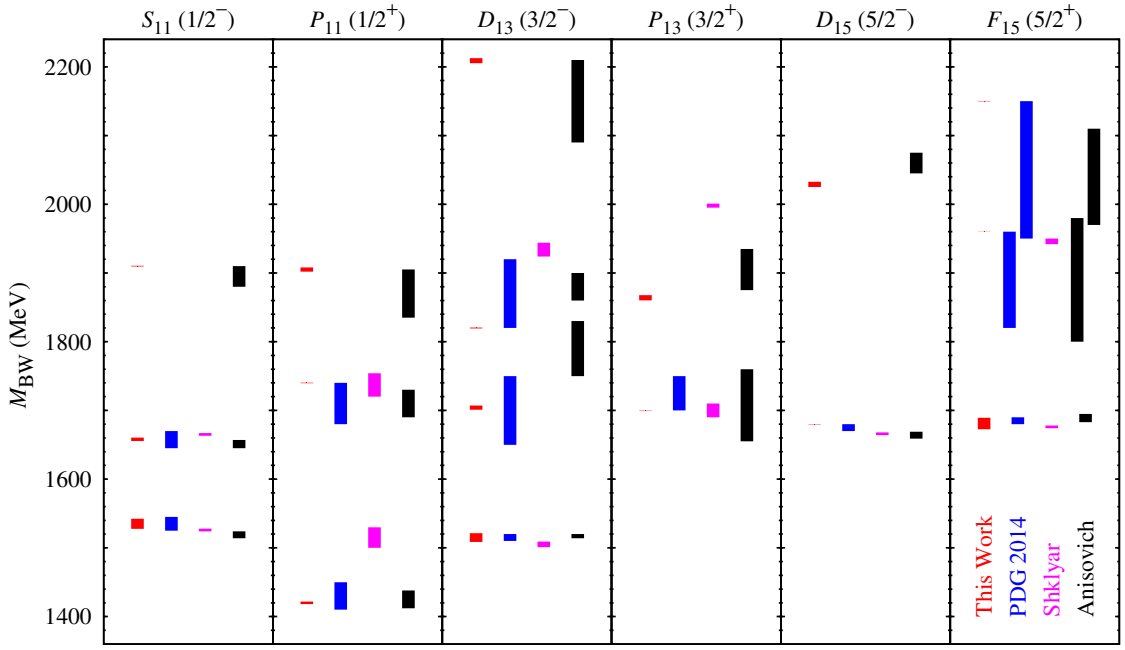

FIG. 17 (color online). The Breit–Wigner resonance masses obtained in the present work compared with those obtained by the Giessen model (Shklyar *et al.* [58]), the Bonn–Gatchina model (Anisovich *et al.* [59]), as well as those estimated by the PDG [7].

Our best model shows the best agreement with the data for $1.70 \lesssim W \lesssim 2.00$ GeV, whereas in the other energy regions, the Bonn–Gatchina analysis exhibits the best agreement.

Compared to other observables, the target asymmetry has fewer experimental data. Clearly, the agreement with experimental data is rather difficult to achieve during the fit process due to the competition with other observables that have more data points and smaller error bars. Nevertheless, as shown in Fig. 22, our best model can still fit the data for $W \gtrsim 1.7$ GeV. In the lower energy region, both the Bonn–Gatchina and

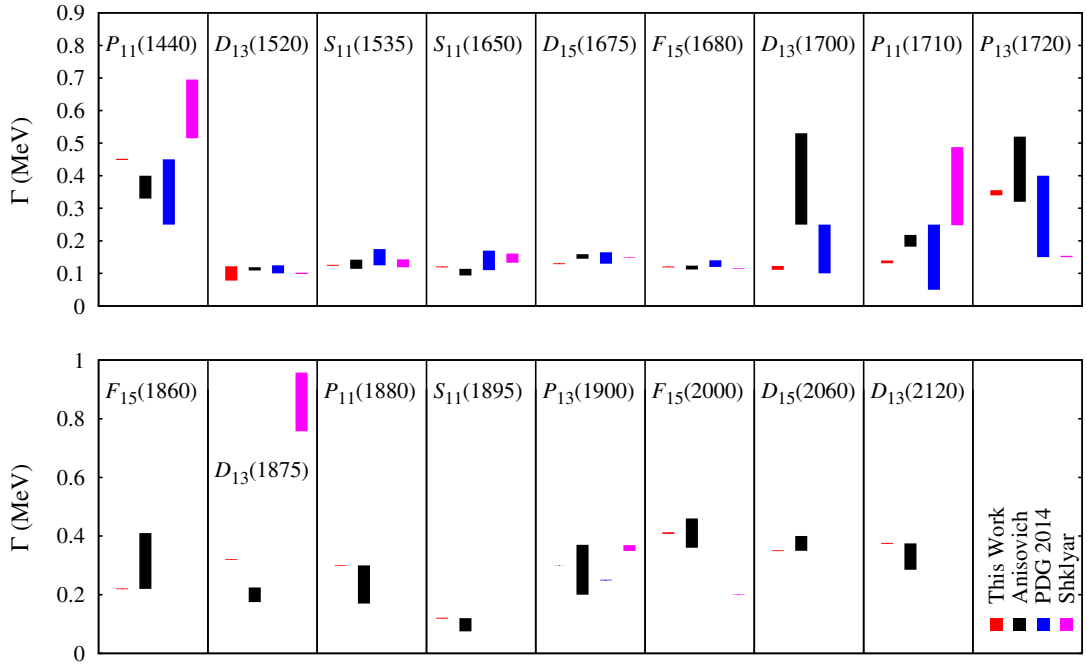

FIG. 18 (color online). As in Fig. 17, but for the extracted nucleon resonance widths.

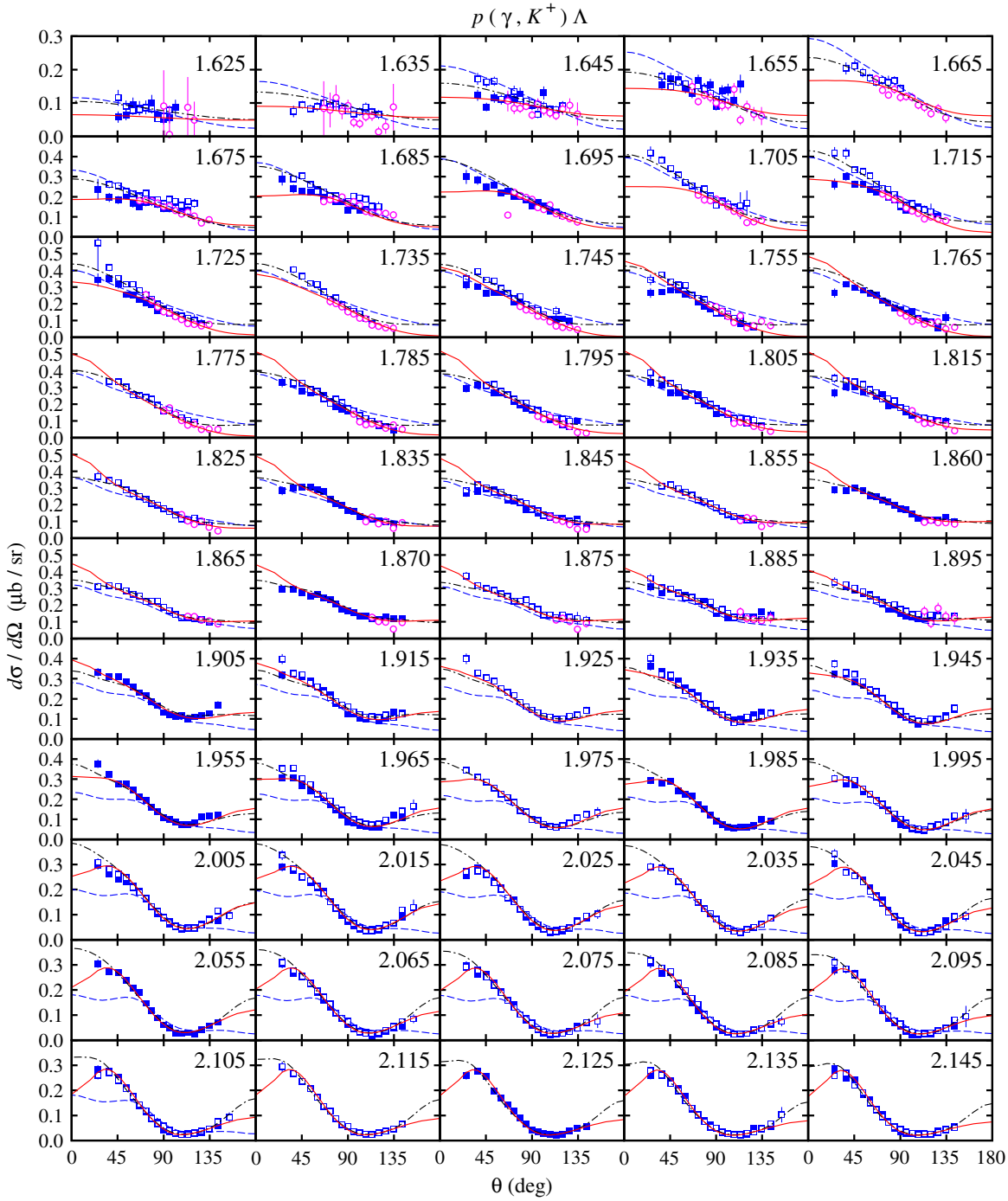

FIG. 19 (color online). Comparison between differential cross sections obtained from the best model of the present work (Model D, solid lines), the Bonn–Gatchina partial wave analysis (dash-dotted lines) [59], and the ANL-Osaka dynamical coupled-channel analysis (dashed lines) [1]. Notation for experimental data is as in Fig. 4.

ANL-Osaka models exhibit a better agreement, whereas our model can only reproduce the shape (or sign). It is also important to note that in the high-energy region all models cannot reproduce the data at backward angles. We hope that the new measurement performed by the FROST Collaboration at Jefferson Laboratory (JLab) can settle this problem in the future [60].

The beam-recoil polarizations C_x and C_z are shown in Fig. 23. Our present analysis can nicely reproduce the C_x data in the low-energy region, whereas in the higher energy region the Bonn–Gatchina model exhibits a better agreement. On the other hand, for the C_z observable, our model shows good agreement with experimental data, except near the threshold, where all models fail to

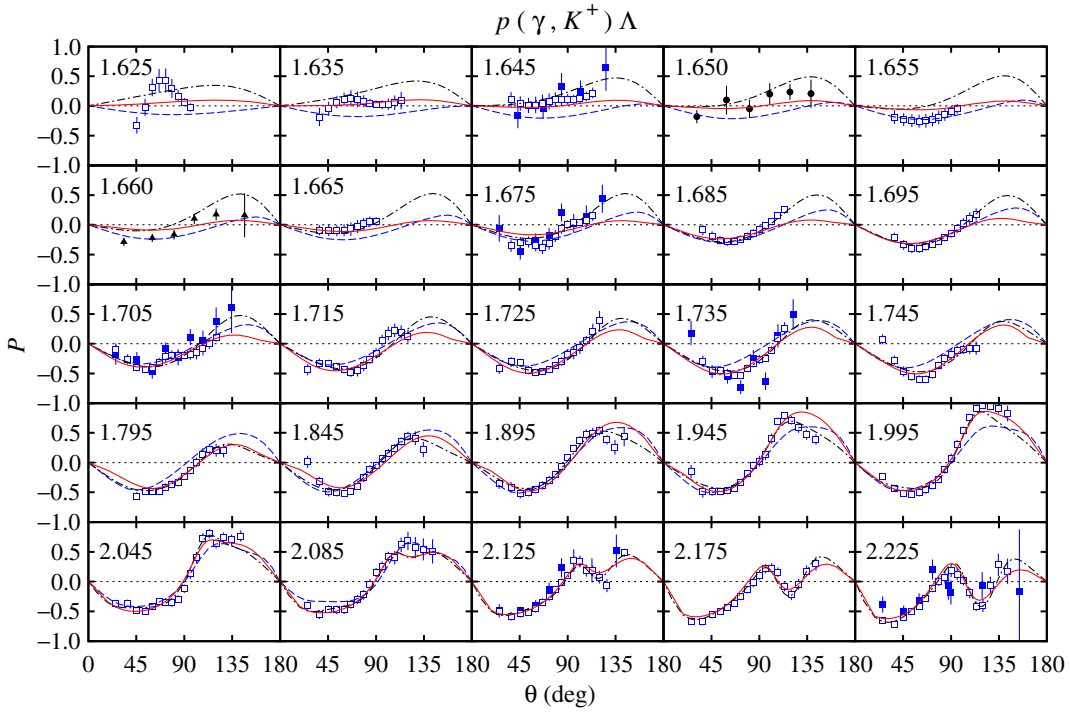

FIG. 20 (color online). As in Fig. 19, but for the recoiled Λ polarization.

reproduce the structures shown by the data at this kinematics.

As shown in the previous section, Model D tends to produce small polarization observables at the threshold region except for C_z, where the polarization is $+1$ at this kinematics (see Figs. 8–13). Therefore, a sudden increase of these observables near the threshold region is difficult to achieve by Model D. This behavior also appears in the case of photon-recoil double polarization O_x and O_z as shown in Fig. 24. Nevertheless, for other kinematical regions, we can see that our model fits the data nicely, except in the case where other phenomenological models

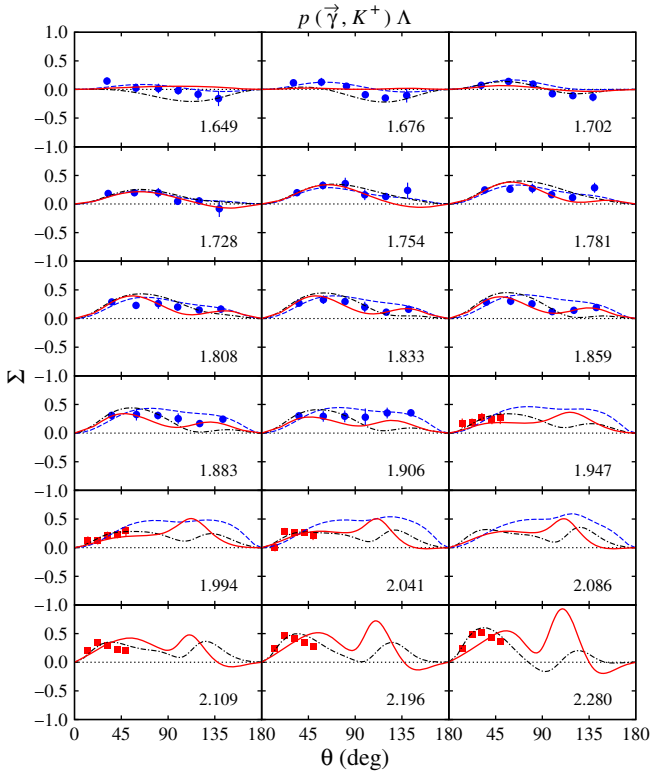

FIG. 21 (color online). As in Fig. 19, but for the photon asymmetry.

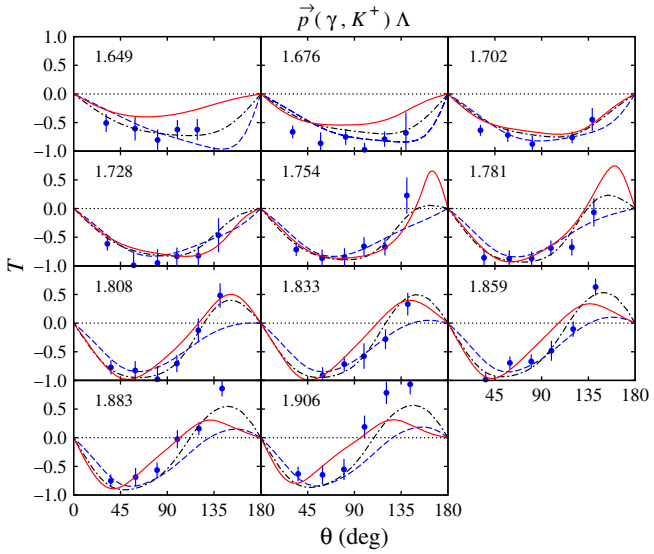

FIG. 22 (color online). As in Fig. 19, but for the target asymmetry.

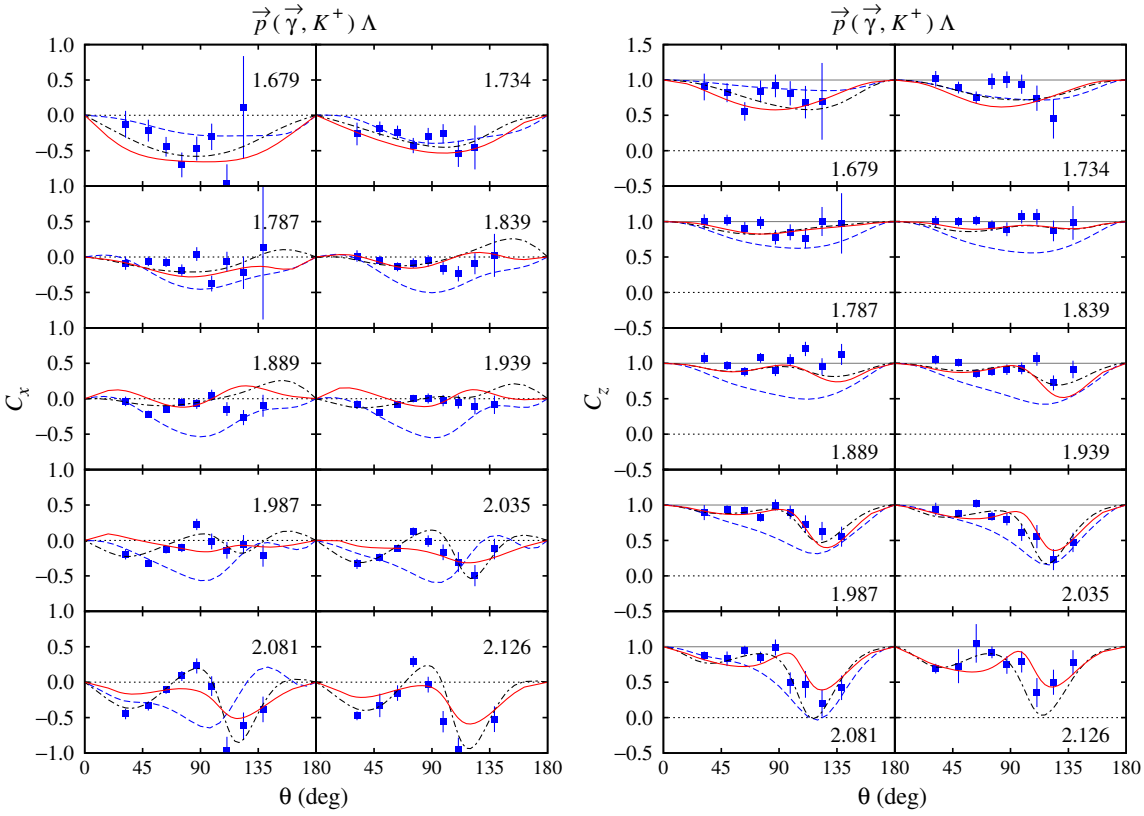

FIG. 23 (color online). As in Fig. 19, but for the photon-recoil double polarization C_x and C_z.

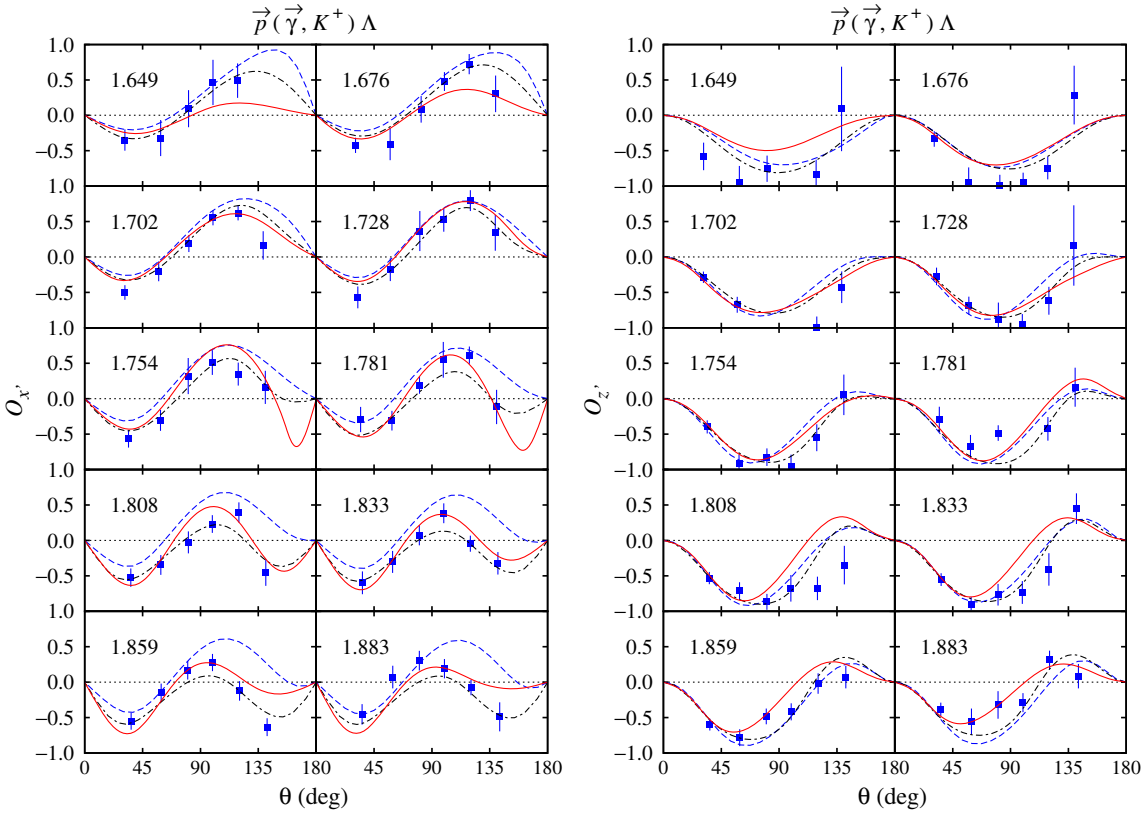

FIG. 24 (color online). As in Fig. 19, but for the photon-recoil double polarization O_x and O_z.

also fail to reproduce experimental data, e.g., for $O_{z'}$ at $W = 1.808$ GeV.

VII. CGLN AMPLITUDES AND EXTRACTED MULTIPOLES

The CGLN amplitudes for the isobar models described in the present work can be directly calculated from the amplitudes A_i given by Eq. (3), i.e., [61,62],

$$\bar{u}_\Lambda \sum_{i=1}^{6} A_i(s,t,u,k^2) M_i u_p = \chi_f^\dagger \mathcal{F} \chi_i, \tag{59}$$

where

$$\mathcal{F} = \boldsymbol{\sigma}\cdot\boldsymbol{b} F_1 - i\boldsymbol{\sigma}\cdot\hat{\boldsymbol{q}}\boldsymbol{\sigma}\cdot(\hat{\boldsymbol{k}}\times\boldsymbol{b})F_2 + \boldsymbol{\sigma}\cdot\hat{\boldsymbol{k}}\,\hat{\boldsymbol{q}}\cdot\boldsymbol{b}F_3 + \boldsymbol{\sigma}\cdot\hat{\boldsymbol{q}}\,\hat{\boldsymbol{q}}\cdot\boldsymbol{b}F_4 - \boldsymbol{\sigma}\cdot\hat{\boldsymbol{q}}b_0F_5 - \boldsymbol{\sigma}\cdot\hat{\boldsymbol{k}}b_0F_6 \tag{60}$$

with

$$b_\mu = \epsilon_\mu - \frac{\hat{\boldsymbol{k}}\cdot\epsilon}{|\boldsymbol{k}|}k_\mu. \tag{61}$$

For the photoproduction of the kaon, only $F_1, \ldots, F_4$ exist, and their relations to A_i are given by [23,28,62]

$$F_{1,2} = \frac{1}{8\pi W}[(E_p \pm m_p)(E_\Lambda \pm m_\Lambda)]^{1/2} \times [\pm(W\mp m_p)A_1 + q_K\cdot k(A_3 - A_4) + (W\mp m_p)(W\mp m_\Lambda)A_4], \tag{62}$$

$$F_{3,4} = \frac{|\boldsymbol{q}_K||\boldsymbol{k}|}{8\pi W}\left(\frac{E_\Lambda \pm m_\Lambda}{E_p \pm m_p}\right)^{1/2}[\pm(s - m_p^2)A_2 + (W \pm m_p)(A_3 - A_4)]. \tag{63}$$

The calculated CGLN amplitudes obtained from Eqs. (62) and (63) will be compared with those obtained from the Kaon–Maid and the Bonn–Gatchina models. For the Kaon–Maid model, the amplitudes are obtained directly from its homepage [63]. Since the homepage for the Bonn–Gatchina model [64] does not provide the CGLN amplitudes for the kaon photoproduction, we can directly calculate the amplitudes by using the provided multipoles, i.e.,

$$\begin{aligned}
F_1 = {} & E_{0+} + E_{2-} + 3M_{2-} - \frac{3}{2}(E_{2+} + 2M_{2+}) - \frac{3}{2}(E_{4-} + 5M_{4-}) + \frac{15}{8}(E_{4+} + 4M_{4+}) + \frac{15}{8}(E_{6-} + 7M_{6-}) \\
& - \frac{35}{16}(E_{6+} + 6M_{6+}) - \frac{35}{16}(E_{8-} + 9M_{8-}) + \frac{315}{128}(E_{8+} + 8M_{8+}) + \Big\{3(E_{1+} + M_{1+}) + 3(E_{3-} + 4M_{3-}) \\
& - \frac{15}{2}(E_{3+} + 3M_{3+}) - \frac{15}{2}(E_{5-} + 6M_{5-}) + \frac{105}{8}(E_{5+} + 5M_{5+}) + \frac{105}{8}(E_{7-} + 8M_{7-}) - \frac{315}{16}(E_{7+} + 7M_{7+}) \\
& - \frac{315}{16}(E_{9-} + 10M_{9-}) + \frac{3465}{128}(E_{9+} + 9M_{9+})\Big\}\cos\theta + \Big\{\frac{15}{2}(E_{2+} + 2M_{2+}) + \frac{15}{2}(E_{4-} + 5M_{4-}) - \frac{105}{4}(E_{4+} \\
& + 4M_{4+}) - \frac{105}{4}(E_{6-} + 7M_{6-}) + \frac{945}{16}(E_{6+} + 6M_{6+}) + \frac{945}{16}(E_{8-} + 9M_{8-}) - \frac{3465}{32}(E_{8+} + 8M_{8+})\Big\}\cos^2\theta \\
& + \Big\{\frac{35}{2}(E_{3+} + 3M_{3+}) + \frac{35}{2}(E_{5-} + 6M_{5-}) - \frac{315}{4}(E_{5+} + 5M_{5+}) - \frac{315}{4}(E_{7-} + 8M_{7-}) + \frac{3465}{16}(E_{7+} + 7M_{7+}) \\
& + \frac{3465}{16}(E_{9-} + 10M_{9-}) - \frac{15015}{32}(E_{9+} + 9M_{9+})\Big\}\cos^3\theta + \Big\{\frac{315}{8}(E_{4+} + 4M_{4+}) + \frac{315}{8}(E_{6-} + 7M_{6-}) \\
& - \frac{3465}{16}(E_{6+} + 6M_{6+}) - \frac{3465}{16}(E_{8-} + 9M_{8-}) + \frac{45045}{64}(E_{8+} + 8M_{8+})\Big\}\cos^4\theta + \Big\{\frac{693}{8}(E_{5+} + 5M_{5+}) \\
& + \frac{693}{8}(E_{7-} + 8M_{7-}) - \frac{9009}{16}(E_{7+} + 7M_{7+}) - \frac{9009}{16}(E_{9-} + 10M_{9-}) + \frac{135135}{64}(E_{9+} + 9M_{9+})\Big\}\cos^5\theta \\
& + \Big\{\frac{3003}{16}(E_{6+} + 6M_{6+}) + \frac{3003}{16}(E_{8-} + 9M_{8-}) - \frac{45045}{32}(E_{8+} + 8M_{8+})\Big\}\cos^6\theta + \Big\{\frac{6435}{16}(E_{7+} + 7M_{7+}) \\
& + \frac{6435}{16}(E_{9-} + 10M_{9-}) - \frac{109395}{32}(E_{9+} + 9M_{9+})\Big\}\cos^7\theta + \frac{109395}{128}(E_{8+} + 8M_{8+})\cos^8\theta \\
& + \frac{230945}{128}(E_{9+} + 9M_{9+})\cos^9\theta
\end{aligned} \tag{64}$$

$$
\begin{aligned}
F_2 = {} & M_{1-} + 2M_{1+} - \frac{3}{2}(3M_{3-} + 4M_{3+}) + \frac{15}{8}(5M_{5-} + 6M_{5+}) - \frac{35}{16}(7M_{7-} + 8M_{7+}) + \frac{315}{128}(9M_{9-} + 10M_{9+}) \\
& + \left\{3(2M_{2-} + 3M_{2+}) - \frac{15}{2}(4M_{4-} + 5M_{4+}) + \frac{105}{8}(6M_{6-} + 7M_{6+}) - \frac{315}{16}(8M_{8-} + 9M_{8+})\right\}\cos\theta \\
& + \left\{\frac{15}{2}(3M_{3-} + 4M_{3+}) - \frac{105}{4}(5M_{5-} + 6M_{5+}) + \frac{945}{16}(7M_{7-} + 8M_{7+}) - \frac{3465}{32}(9M_{9-} + 10M_{9+})\right\}\cos^2\theta \\
& + \left\{\frac{35}{2}(4M_{4-} + 5M_{4+}) - \frac{315}{4}(6M_{6-} + 7M_{6+}) + \frac{3465}{16}(8M_{8-} + 9M_{8+})\right\}\cos^3\theta \\
& + \left\{\frac{315}{8}(5M_{5-} + 6M_{5+}) - \frac{3465}{16}(7M_{7-} + 8M_{7+}) + \frac{45045}{64}(9M_{9-} + 10M_{9+})\right\}\cos^4\theta \\
& + \left\{\frac{693}{8}(6M_{6-} + 7M_{6+}) - \frac{9009}{16}(8M_{8-} + 9M_{8+})\right\} \\
& \times \cos^5\theta + \left\{\frac{3003}{16}(7M_{7-} + 8M_{7+}) - \frac{45045}{32}(9M_{9-} + 10M_{9+})\right\}\cos^6\theta \\
& + \left\{\frac{6435}{16}(8M_{8-} + 9M_{8+})\right\}\cos^7\theta \\
& + \left\{\frac{109395}{128}(9M_{9-} + 10M_{9+})\right\}\cos^8\theta
\end{aligned} \tag{65}
$$

$$
\begin{aligned}
F_3 = {} & 3(E_{1+} - M_{1+}) + 3(E_{3-} + M_{3-}) - \frac{15}{2}(E_{3+} - M_{3+}) - \frac{15}{2}(E_{5-} + M_{5-}) + \frac{105}{8}(E_{5+} - M_{5+}) \\
& + \frac{105}{8}(E_{7-} + M_{7-}) - \frac{315}{16}(E_{7+} - M_{7+}) - \frac{315}{16}(E_{9-} + M_{9-}) + \frac{3465}{128}(E_{9+} - M_{9+}) \\
& + \left\{15(E_{2+} - M_{2+}) + 15(E_{4-} + M_{4-}) - \frac{105}{2}(E_{4+} - M_{4+}) - \frac{105}{2}(E_{6-} + M_{6-})\right. \\
& \left. + \frac{945}{8}(E_{6+} - M_{6+}) + \frac{945}{8}(E_{8-} + M_{8-}) - \frac{3465}{16}(E_{8+} - M_{8+})\right\}\cos\theta \\
& + \left\{\frac{105}{2}(E_{3+} - M_{3+}) + \frac{105}{2}(E_{5-} + M_{5-}) - \frac{945}{4}(E_{5+} - M_{5+})\right. \\
& \left. - \frac{945}{4}(E_{7-} + M_{7-}) + \frac{10395}{16}(E_{7+} - M_{7+}) + \frac{10395}{16}(E_{9-} + M_{9-}) - \frac{45045}{32}(E_{9+} - M_{9+})\right\}\cos^2\theta \\
& + \left\{\frac{315}{2}(E_{4+} - M_{4+}) + \frac{315}{2}(E_{6-} + M_{6-}) - \frac{3465}{4}(E_{6+} - M_{6+})\right. \\
& \left. - \frac{3465}{4}(E_{8-} + M_{8-}) + \frac{45045}{16}(E_{8+} - M_{8+})\right\}\cos^3\theta \\
& + \left\{\frac{3465}{8}(E_{5+} - M_{5+}) + \frac{3465}{8}(E_{7-} + M_{7-}) - \frac{45045}{16}(E_{7+} - M_{7+})\right. \\
& \left. - \frac{45045}{16}(E_{9-} + M_{9-}) + \frac{675675}{64}(E_{9+} - M_{9+})\right\}\cos^4\theta \\
& + \left\{\frac{9009}{8}(E_{6+} - M_{6+}) + \frac{9009}{8}(E_{8-} + M_{8-}) - \frac{135135}{16}(E_{8+} - M_{8+})\right\}\cos^5\theta \\
& + \left\{\frac{45045}{16}(E_{7+} - M_{7+}) + \frac{45045}{16}(E_{9-} + M_{9-}) - \frac{765765}{32}(E_{9+} - M_{9+})\right\}\cos^6\theta \\
& + \left\{\frac{109395}{16}(E_{8+} - M_{8+})\right\}\cos^7\theta + \left\{\frac{2078505}{128}(E_{9+} - M_{9+})\right\}\cos^8\theta
\end{aligned} \tag{66}
$$

$$F_4 = 3(M_{2+} - E_{2+} - M_{2-} - E_{2-}) - \frac{15}{2}(M_{4+} - E_{4+} - M_{4-} - E_{4-}) + \frac{105}{8}(M_{6+} - E_{6+} - M_{6-} - E_{6-}) - \frac{315}{16}(M_{8+} - E_{8+} - M_{8-} - E_{8-}) + \left\{15(M_{3+} - E_{3+} - M_{3-} - E_{3-}) - \frac{105}{2}(M_{5+} - E_{5+} - M_{5-} - E_{5-}) + \frac{945}{8}(M_{7+} - E_{7+} - M_{7-} - E_{7-}) - \frac{3465}{16}(M_{9+} - E_{9+} - M_{9-} - E_{9-})\right\}\cos\theta + \left\{\frac{105}{2}(M_{4+} - E_{4+} - M_{4-} - E_{4-}) - \frac{945}{4}(M_{6+} - E_{6+} - M_{6-} - E_{6-}) + \frac{10395}{16}(M_{8+} - E_{8+} - M_{8-} - E_{8-})\right\}\cos^2\theta + \left\{\frac{315}{2}(M_{5+} - E_{5+} - M_{5-} - E_{5-}) - \frac{3465}{4}(M_{7+} - E_{7+} - M_{7-} - E_{7-}) + \frac{45045}{16}(M_{9+} - E_{9+} - M_{9-} - E_{9-})\right\}\cos^3\theta + \left\{\frac{3465}{8}(M_{6+} - E_{6+} - M_{6-} - E_{6-}) - \frac{45045}{16}(M_{8+} - E_{8+} - M_{8-} - E_{8-})\right\}\cos^4\theta + \left\{\frac{9009}{8}(M_{7+} - E_{7+} - M_{7-} - E_{7-}) - \frac{135135}{16}(M_{9+} - E_{9+} - M_{9-} - E_{9-})\right\}\cos^5\theta + \left\{\frac{45045}{16}(M_{8+} - E_{8+} - M_{8-} - E_{8-})\right\}\cos^6\theta + \left\{\frac{109395}{16}(M_{9+} - E_{9+} - M_{9-} - E_{9-})\right\}\cos^7\theta. \quad (67)$$

The calculated CGLN amplitudes, $F_1 \ldots F_4$, obtained from Model D, Bonn–Gatchina, and Kaon–Maid calculations are shown in Fig. 25. It is obvious that the amplitude obtained from these models cannot be identical because they depend on the number of resonances used in the model and the fitted experimental database, while it is clear that the models utilize different nucleon resonances and were fitted to different experimental databases. Nevertheless, we expect to observe a consistent behavior of the amplitudes, and if the models gives different values for a certain amplitude, then this must be compensated by different values of other amplitudes.

In general, all models indicate a similar angular distribution of the amplitudes in the low-energy region, whereas in the high-energy region, the models show different amplitudes for certain kinematics. Presumably, this originates from the fact that all three models utilize a similar combination of low mass nucleon resonances. For the higher mass nucleon resonances, both the number of resonances and the resonance properties used in the models are quite different. Therefore, it is natural if more variations would be expected for higher energies as shown in Fig. 25. Especially remarkable is the real part of F_1 obtained for Model D (solid line) at a forward angle, where its value changes significantly as the energy increases above 1.8 GeV. We have noted that the real part of this amplitude changes its sign at $W \approx 1.890$ GeV. On the other hand, the real part of F_2 also changes at this energy, and therefore we could expect that the observables obtained from the combined contribution are comparable to other models.

The CGLN amplitudes shown in Fig. 25 are obviously consistent with the calculated electric and magnetic multipoles given in Fig. 26 (will be discussed later), since in the low-energy region the amplitudes exhibit almost a linear function of $\cos\theta$. This can be understood from Eqs. (64)–(67), where we can see that the low momentum angular multipoles (with $l \leq 1$) only contribute to the terms proportional to 1 or $\cos\theta$. From Fig. 26, it is apparent that the low momentum angular multipoles are only significant at low energies.

Comparison between the extracted multipoles could reveal more information compared to the comparison of the CGLN amplitudes discussed above. Moreover, both the Kaon–Maid as well as the Bonn–Gatchina models provide an interactive program for calculating the multipoles at their homepages [63,64]. The relations between these multipoles and the CGLN amplitudes are given, e.g., in Ref. [28]. To facilitate the reader, we, however, represent these relations in this paper, which are used to calculate the multipoles shown by the solid lines in Fig. 26. Since we only need the photoproduction multipoles, only four relations are needed to calculate the multipoles from Model D, i.e., [28],

$$E_{l+} = \int_{-1}^{+1} dx \left[\frac{1}{2(l+1)}P_l F_1 - \frac{1}{2(l+1)}P_{l+1}F_2 + \frac{l}{2(l+1)(2l+1)}(P_{l-1} - P_{l+1})F_3 + \frac{1}{2(2l+3)}(P_l - P_{l+2})F_4\right], \quad (68)$$

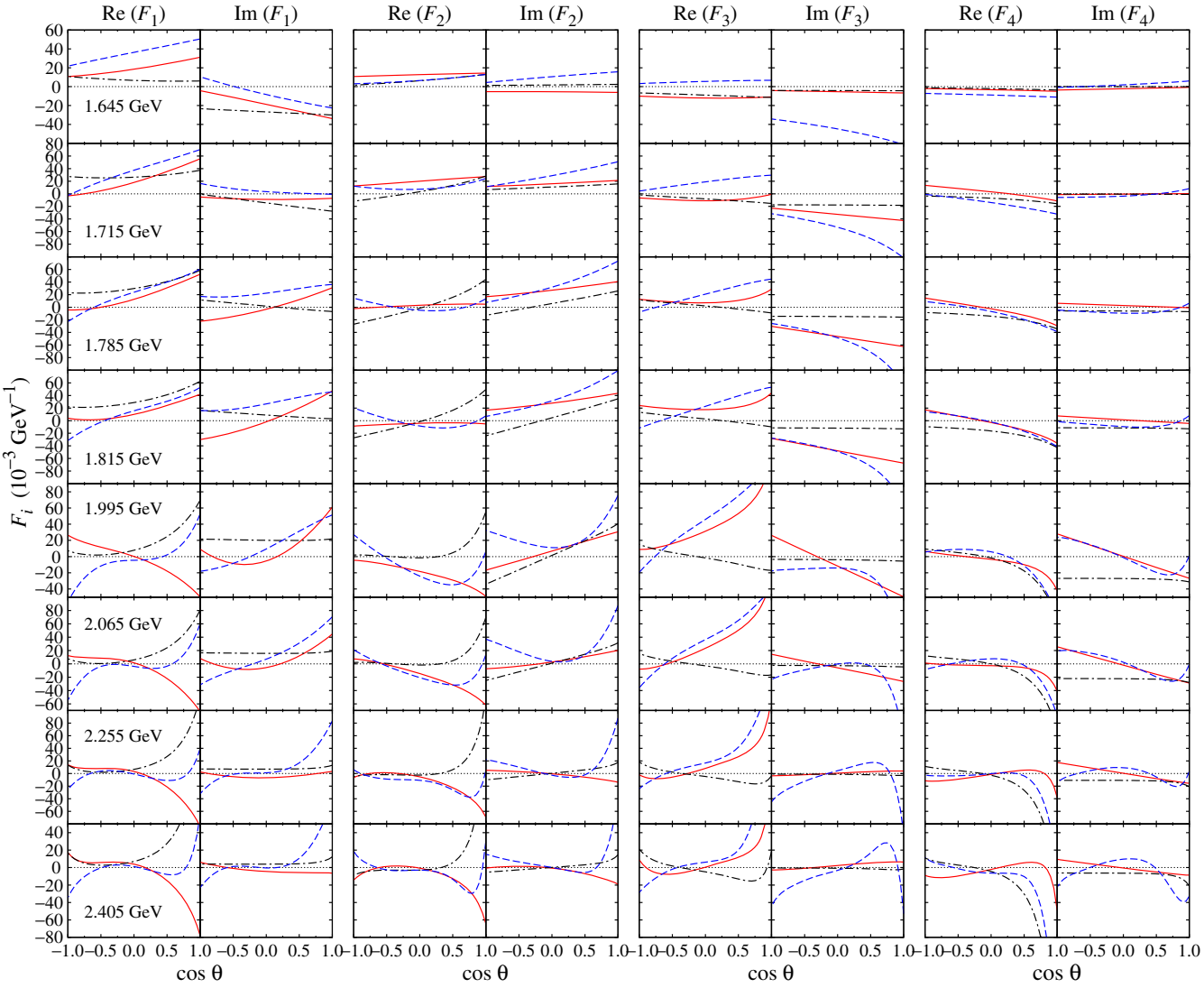

FIG. 25 (color online). Angular distribution of the CGLN amplitudes for different values of the total c.m. energy W. Solid lines indicate the result obtained from the present analysis, whereas the dashed and the dash-dotted lines are obtained from the Bonn–Gatchina and Kaon–Maid models, respectively.

$$E_{l-} = \int_{-1}^{+1} dx \left[\frac{1}{2l} P_l F_1 - \frac{1}{2l} P_{l-1} F_2 + \frac{l+1}{2l(2l+1)} (P_{l+1} - P_{l-1}) F_3 + \frac{1}{2(2l-1)} (P_l - P_{l-2}) F_4 \right], \tag{69}$$

$$M_{l+} = \int_{-1}^{+1} dx \left[\frac{1}{2(l+1)} P_l F_1 - \frac{1}{2(l+1)} P_{l+1} F_2 + \frac{l}{2(l+1)(2l+1)} (P_{l+1} - P_{l-1}) F_3 \right], \tag{70}$$

$$M_{l-} = \int_{-1}^{+1} dx \left[-\frac{1}{2l} P_l F_1 + \frac{1}{2l} P_{l-1} F_2 + \frac{1}{2l(2l+1)} (P_{l-1} - P_{l+1}) F_3 \right], \tag{71}$$

where $x = \cos\theta$ and both P_l and F_i are functions of x. The Bonn–Gatchina and Kaon–Maid multipoles are obtained directly from their homepages [63,64].

As in the case of the CGLN amplitudes, it is apparent that the values of the multipoles given in Eqs. (68)–(71) depend on the number of nucleon resonances included in the models, as well as the experimental data used in the fits. Comparison between the multipoles obtained from Model D, along with the Bonn–Gathcina [64] and Kaon–Maid [63] models, shown in Fig. 26 proves this. In fact, in Ref. [29], it is shown that fitting a model to different databases, i.e., SAPHIR [49] and CLAS [41] ones, leads to very different values of multipoles. Note that, since the number of nucleon resonances used in Kaon–Maid is much less than that of the other two models, not all multipoles shown in Fig. 26 can be compared with the Kaon–Maid model. On the other

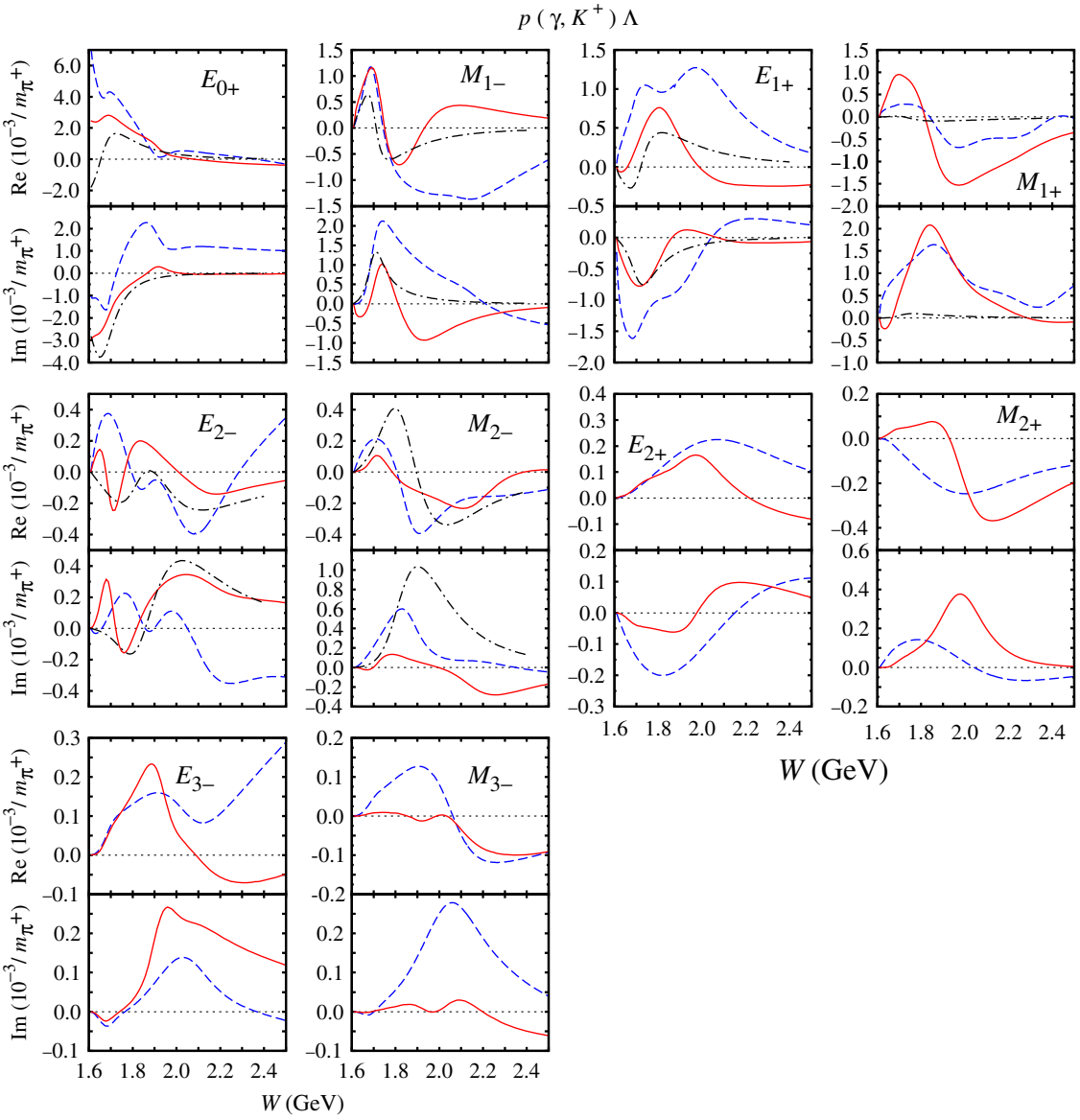

FIG. 26 (color online). Electric and magnetic multipoles of the nucleon resonances used in the present analysis. Notation of the curves is as in Fig. 25.

hand, only a small number of Bonn–Gatchina multipoles are displayed in this figure (i.e., $l \leq 3$).

However, although the three different models exhibit different energy distributions of multipoles, it is remarkable that the general pattern of the multipoles seems to be consistent. In some cases, e.g., E_{0+}, E_{1+}, and E_{2-}, we can observe that the Bonn–Gathcina model displays more structures in their multipoles because more nucleon resonances are involved.

For the low spin state, e.g., we can see in Fig. 26 that the E_{0+} multipole shows the structures near 1660 and 1900 MeV that correspond to the two S_{11} states used in our model, i.e., the $N(1650)$ and $N(1895)$ resonances (see Table VI and Fig. 17). The structures are also exhibited by the Bonn–Gatchina model, whereas only the $N(1650)$ structure is shown by the Kaon-Maid, because the $N(1895)$ resonance is not included. In the M_{1-} multipole, all three models clearly indicate the $N(1710)$, a P_11 state, around 1700 MeV, whereas the $N(1880)$ state creates the structure near 1900 MeV.

To conclude, in spite of the differences found in the magnitude and shapes of certain multipoles, we might say that the calculated multipoles from Model D are still consistent with those obtained from the Bonn–Gatchina model and, to some extent, from Kaon–Maid.

TABLE VI. Extracted resonance mass (m) and width (Γ) from the fit to experimental data for all models considered in the present analysis compared with those of the PDG [7].

m or Γ (MeV)	A	B	C	D	PDG
$m_{N(1440)}$	1470	1420	1420	1420	1430 ± 20
$\Gamma_{N(1440)}$	450	450	450	450	350 ± 100
$m_{N(1520)}$	1515	1515	1515	1515	1515 ± 5
$\Gamma_{N(1520)}$	100	100	125	100	115^{10}_{-15}
$m_{N(1535)}$	1525	1545	1532	1534	1535^{+20}_{-10}
$\Gamma_{N(1535)}$	175	125	125	125	150 ± 25
$m_{N(1650)}$	1645	1670	1670	1657	1655^{+15}_{-10}
$\Gamma_{N(1650)}$	180	180	120	120	140 ± 30
$m_{N(1675)}$	1670	1670	1670	1680	1675 ± 5
$\Gamma_{N(1675)}$	165	165	151	130	150^{+15}_{-20}
$m_{N(1680)}$	1680	1690	1680	1680	1685 ± 5
$\Gamma_{N(1680)}$	120	120	140	120	130 ± 10
$m_{N(1700)}$	1695	1682	1690	1703	1700 ± 50
$\Gamma_{N(1700)}$	164	100	153	117	150^{+100}_{-50}
$m_{N(1710)}$	1704	1680	1690	1740	1710 ± 30
$\Gamma_{N(1710)}$	154	250	74	135	100^{+150}_{-50}
$m_{N(1720)}$	1700	1700	1700	1700	1720^{+30}_{-20}
$\Gamma_{N(1720)}$	400	153	391	347	250^{+150}_{-100}
$m_{N(1860)}$	1820	1820	1960	1960	1860^{+100}_{-40}
$\Gamma_{N(1860)}$	351	410	334	220	270^{+140}_{-50}
$m_{N(1875)}$	1920	1820	1920	1820	1875^{+45}_{-55}
$\Gamma_{N(1875)}$	320	263	193	320	200 ± 25
$m_{N(1880)}$	1835	1905	1835	1905	1870 ± 35
$\Gamma_{N(1880)}$	300	300	170	300	235 ± 65
$m_{N(1895)}$	1880	1894	1880	1910	1895 ± 15
$\Gamma_{N(1895)}$	100	075	115	120	90^{+30}_{-15}
$m_{N(1900)}$	1869	1981	1938	1863	1900
$\Gamma_{N(1900)}$	287	266	259	300	250
$m_{N(2000)}$	2120	2150	2150	2150	2050 ± 100
$\Gamma_{N(2000)}$	410	510	410	410	198 ± 2
$m_{N(2060)}$	1989	2160	1960	2029	2060
$\Gamma_{N(2060)}$	350	350	400	350	375 ± 25
$m_{N(2120)}$	2220	2143	2109	2209	2120
$\Gamma_{N(2120)}$	375	31	375	375	330 ± 45

VIII. SUMMARY AND CONCLUSIONS

We have analyzed the kaon photoproduction process $\gamma + p \to K^+ + \Lambda$ by using isobar models that contain different formulations of spin-3/2 and spin-5/2 propagators and vertices. For this purpose, we have derived the corresponding amplitudes and decomposed them into the standard gauge and Lorentz invariant matrices. The amplitudes are written in a compact form and include also the longitudinal terms. Therefore, our present formalism is useful not only for photoproduction but also for electroproduction. All available nucleon resonances with spins up to 5/2 listed by the PDG are taken into account in the model, and the corresponding coupling constants are extracted by fitting all available kaon photoproduction data, consisting of more than 7000 data points. By using two different formalisms (Models 1 and 2) for spins 3/2 and 5/2, four isobar models (Models A, B, C, and D) are available in this analysis. It is found that the use of the spin-3/2 formalism of Model 1 in Models A and C leads to a serious problem in reproducing the experimental data, whereas Model D that utilizes the gauge-invariant formulation of the spin-3/2 and −5/2 interactions yields the best agreement with experimental data. The results obtained from Model D have been also compared to those obtained from previous analyses. It is found that Model D provides a good description of experimental data, comparable with the previous analyses. The same conclusion can be also drawn from the comparison of the calculated CGLN amplitudes and multipoles.

ACKNOWLEDGMENTS

We thank Hiroyuki Kamano for providing us the numerical data for plots of the ANL-Osaka dynamical coupled-channel analysis. Useful discussions with Petr Bydžovský and Lothar Tiator are also gratefully acknowledged. This work has been partly supported by the Research-Cluster-Grant-Program of the University of Indonesia, under Contract No. 1862/UN.R12/HKP.05.00/2015.

APPENDIX A: SPIN-3/2 AND −5/2 RESONANCE AMPLITUDES FOR MODEL 1

1. Amplitudes for the spin-3/2 resonances

$$A_1 = \pm\left[(m_p+m_\Lambda)\left(\frac{3}{2}-\frac{1}{s}c_\Lambda \pm \frac{1}{2\sqrt{s}}m_\Lambda\right) \mp c_\pm\{s-m_K^2-3b_\Lambda+m_\Lambda(\pm 2\sqrt{s}+m_p)\} \mp \frac{2}{s}c_\Lambda c_\pm c_k \pm \frac{1}{\sqrt{s}}c_\pm \right.$$
$$\left. \times (m_\Lambda c_k + m_\Lambda c_\Lambda - m_p c_\Lambda)\right] G_1 \mp \left[\frac{1}{2}(m_p+m_\Lambda)\left\{b_p - 3b_\Lambda + 2c_\Lambda + m_\Lambda(\pm\sqrt{s}-m_p) + \frac{2}{s}k^2 c_\Lambda \right.\right.$$
$$\left.\left. \mp \frac{1}{\sqrt{s}}[k^2 m_\Lambda \pm c_\Lambda(\sqrt{s}\pm m_p)]\right\} + b_p\left(m_p \mp \frac{1}{\sqrt{s}}c_\Lambda\right)\right] G_2 \pm k^2\left[\frac{1}{2s}(m_p+m_\Lambda)(2c_\Lambda - s \mp m_\Lambda\sqrt{s}) - m_p \pm \frac{1}{\sqrt{s}}c_\Lambda\right] G_3, \quad \text{(A1)}$$

$$A_2 = \frac{1}{t-m_K^2}\left[\left\{3c_\pm(c_4-2b_\Lambda)\pm 2m_\Lambda+\frac{2}{s}c_\pm c_\Lambda(2c_k-s+m_p^2)\mp\frac{1}{\sqrt{s}}m_\Lambda c_\pm[(\sqrt{s}\pm m_p)^2+2c_k]\right\}G_1\right.$$
$$+\left\{3(b_\Lambda-b_p)(\sqrt{s}\mp m_p)+k^2\left[\pm m_\Lambda-\frac{2}{s}c_\Lambda c_\pm(s-m_p^2)-\frac{1}{\sqrt{s}}c_\Lambda\mp\frac{1}{\sqrt{s}}m_\Lambda(\sqrt{s}\pm m_p)\right]\right\}G_2$$
$$\left.+k^2\left\{-3(\sqrt{s}\mp m_p)\mp 2m_\Lambda+\frac{2}{s}c_\pm c_\Lambda(s-m_p^2)\pm\frac{1}{\sqrt{s}}m_\Lambda(\sqrt{s}\pm m_p)\right\}G_3\right], \tag{A2}$$

$$A_3 = \mp\frac{1}{2}\left\{3\mp 2c_\pm m_\Lambda+\frac{2}{s}c_\Lambda\mp\frac{1}{\sqrt{s}}(m_\Lambda\pm 2c_\pm c_\Lambda)\right\}G_1\pm\frac{1}{2}\left[3(b_p+b_\Lambda)-2c_\Lambda\mp c_\pm m_\Lambda(s-m_p^2)-\frac{2}{s}k^2c_\Lambda\right.$$
$$\left.\pm\frac{1}{\sqrt{s}}\{k^2m_\Lambda\pm c_\Lambda(\sqrt{s}\pm m_p)\}\right]G_2\pm\frac{1}{2}k^2\left(3+\frac{2}{s}c_\Lambda\mp\frac{1}{\sqrt{s}}m_\Lambda\right)G_3, \tag{A3}$$

$$A_4 = \pm\frac{1}{2}\left\{3\pm 2c_\pm m_\Lambda-\frac{2}{s}c_\Lambda\pm\frac{1}{\sqrt{s}}(m_\Lambda\pm 2c_\pm c_\Lambda)\right\}G_1\mp\frac{1}{2}\left[3(b_p-b_\Lambda)+2c_\Lambda\pm c_\pm m_\Lambda(s-m_p^2)+\frac{2}{s}k^2c_\Lambda\right.$$
$$\left.\mp\frac{1}{\sqrt{s}}\{k^2m_\Lambda\pm c_\Lambda(\sqrt{s}\pm m_p)\}\right]G_2\mp\frac{1}{2}k^2\left(3-\frac{2}{s}c_\Lambda\pm\frac{1}{\sqrt{s}}m_\Lambda\right)G_3, \tag{A4}$$

$$A_5 = \frac{1}{t-m_K^2}\left[\left\{c_\pm\left(2b_q+b_p-b_\Lambda-\frac{1}{2}k^2\right)+\frac{1}{2}c_5\times\left(\pm\frac{1}{\sqrt{s}}c_\pm m_\Lambda-\frac{2}{s}c_\Lambda c_\pm\right)\right\}G_1+\left\{-\frac{3}{2}(\sqrt{s}\mp m_p)\right.\right.$$
$$\times(b_p+b_\Lambda)\pm\frac{1}{2}c_5\left[\frac{1}{\sqrt{s}}c_\Lambda\pm\frac{1}{\sqrt{s}}m_\Lambda(\sqrt{s}\pm m_p)+\frac{2}{s}c_\Lambda c_\pm(s-m_p^2)\mp m_\Lambda\right]\Big\}G_2+\left\{3(\sqrt{s}\mp m_p)\right.$$
$$\left.\left.\times\left(2b_\Lambda-\frac{1}{2}k^2\right)\pm\frac{1}{2}c_5\left\{m_\Lambda\mp\frac{1}{\sqrt{s}}m_\Lambda m_p\mp\frac{2}{s}c_\Lambda(\sqrt{s}\mp m_p)\right\}\right\}G_3\right], \tag{A5}$$

$$A_6 = \pm\left[\frac{1}{s}c_\Lambda-\frac{3}{2}+\frac{1}{\sqrt{s}}\left\{c_\pm(c_k-m_pm_\Lambda)\pm\frac{1}{2}m_\Lambda\right\}\right]G_1\pm\left[\frac{3}{2}(b_p+b_\Lambda)-c_\Lambda+(\sqrt{s}\mp m_p)\left\{\mp\frac{1}{2}m_\Lambda\pm\frac{1}{2\sqrt{s}}\right.\right.$$
$$\left.\left.\times[m_\Lambda(\sqrt{s}\mp m_p)\pm c_\Lambda]\right\}-\frac{1}{s}c_\Lambda(s-m_p^2)\right]G_2\pm\left[\frac{3}{2}(k^2-2b_\Lambda)+2c_\Lambda+\frac{1}{s}c_\Lambda(s-m_p^2)\pm m_\Lambda(\sqrt{s}\right.$$
$$\left.\mp m_p)\mp\frac{1}{2\sqrt{s}}(\sqrt{s}\pm m_p)\{m_\Lambda(\sqrt{s}\mp m_p)\pm c_\Lambda\}\right]G_3, \tag{A6}$$

where

$$G_1 = \frac{ig_{K\Lambda N^*}g^a_{N^*p\gamma}}{3m_{N^*}(s-m_{N^*}^2+im_{N^*}\Gamma_{N^*})}, \tag{A7}$$

$$G_2 = \frac{ig_{K\Lambda N^*}g^b_{N^*p\gamma}c_\pm^2}{3m_{N^*}(s-m_{N^*}^2+im_{N^*}\Gamma_{N^*})}, \tag{A8}$$

$$G_3 = \frac{ig_{K\Lambda N^*}g^c_{N^*p\gamma}c_\pm^2}{3m_{N^*}(s-m_{N^*}^2+im_{N^*}\Gamma_{N^*})}. \tag{A9}$$

Note that the definition of G_1 is slightly different from that of $\mathcal{G}_1$ in Eq. (22), i.e., $G_1 = \mathcal{G}_1k^2$, whereas in Eqs. (23) and (24), $G_2 = \mathcal{G}_2$ and $G_3 = \mathcal{G}_3$, respectively. In the fitting process, the fitted coupling constants in this case are

$$G^{(1)}_{N^*} \equiv g_{K\Lambda N^*}g^a_{N^*p\gamma}, \tag{A10}$$

$$G^{(2)}_{N^*} \equiv g_{K\Lambda N^*}g^b_{N^*p\gamma}, \tag{A11}$$

$$G_{N^*}^{(3)} \equiv g_{K\Lambda N^*} g^c_{N^* p\gamma}. \tag{A12}$$

Therefore, in the photoproduction process, only $G_{N^*}^{(1)}$ and $G_{N^*}^{(2)}$ are relevant, since in the amplitudes $A_1, \ldots, A_4$ the $G_{N^*}^{(3)}$ coupling constant is proportional to k^2, whereas A_5 and A_6 contribute only to the electroproduction process.

2. Amplitudes for the spin-5/2 resonances

$$\begin{aligned} A_1 = {} & \mp[5c_1\{(m_p+m_\Lambda)c_s \mp 2c_\mp c_1\} \mp 2c_2\{c_\mp c_3 \mp \frac{1}{2s}(m_p+m_\Lambda)c_k\} - d_\mp\{2c_1\sqrt{s}[1+2c_\mp(\sqrt{s} \\ & \pm m_\Lambda)] - 4c_1 c_\mp c_k \pm (m_p+m_\Lambda)[c_1 - c_s\sqrt{s}(\sqrt{s}\pm m_p) + c_s c_k]\}]G_1 \pm \Big[(m_p+m_\Lambda)\Big\{5c_1 \\ & \times\left(\frac{1}{s}k^2 c_\Lambda + b_p - b_\Lambda\right) - k^2 c_2\left(\frac{1}{s}c_k - 1\right)\Big\} + d_\mp\{-c_1(2b_p\sqrt{s} + (m_p+m_\Lambda)[\sqrt{s}(m_p \pm \sqrt{s}) \\ & \mp k^2]) \mp (m_p+m_\Lambda)(k^2 c_s - b_q)[\sqrt{s}(\sqrt{s}\pm m_p) - c_k]\}\Big]G_2 \pm k^2\Big[(m_p+m_\Lambda)\left(5c_1 c_s + \frac{1}{s}c_k c_2\right) \\ & + d_\mp\{-2c_1\sqrt{s} \mp c_1(m_p+m_\Lambda) \pm c_s(m_p+m_\Lambda) \times [\sqrt{s}(\sqrt{s}\pm m_p) - c_k]\}\Big]G_3, \end{aligned} \tag{A13}$$

$$\begin{aligned} A_2 = {} & \frac{2}{t-m_K^2}\Bigg(\Big[5c_1\{(\sqrt{s}\pm m_p)c_s - 2c_\mp c_1\} + k^2 c_\mp c_2\left(2 - \frac{1}{s}c_k\right) \pm d_\mp\{c_1 c_\mp(k^2+2c_k) \\ & - c_s(b_p\sqrt{s} \pm m_p c_k)\}\Big]G_1 + \Big[(\sqrt{s}\pm m_p)\Big\{5c_1(k^2 c_s - b_q) + k^2 c_2\left(\frac{1}{s}c_k - 1\right)\Big\} \\ & - d_\mp\{c_1 k^2 m_p \pm (k^2 c_s - b_q)[b_p\sqrt{s} \pm c_k m_p]\}\Big]G_2 - k^2\Big[(\sqrt{s}\pm m_p)\left(5c_1 c_s + \frac{1}{s}c_2 c_k\right) \\ & \mp d_\mp\{c_1(\sqrt{s}\pm m_p) + c_s(b_p\sqrt{s} \pm c_k m_p)\}\Big]G_3\Bigg), \end{aligned} \tag{A14}$$

$$\begin{aligned} A_3 = {} & \pm\Big[5c_1\left(1+\frac{1}{s}c_\Lambda\right) - \frac{1}{s}c_k c_2 \pm d_\mp\Big\{c_1(1+4c_\mp\sqrt{s}) + \left(1+\frac{1}{s}c_\Lambda\right)[b_p \pm m_p(\sqrt{s}\pm m_p)]\Big\}\Big]G_1 \mp \Big[5c_1(2b_p \\ & - b_q + k^2 c_s) + k^2 c_2\left(\frac{1}{s}c_k - 1\right) \mp d_\mp\{c_1[k^2 - \sqrt{s}(\sqrt{s}\pm m_p)] + (2b_p - b_q + k^2 c_s)[c_k - \sqrt{s} \\ & \times(\sqrt{s}\pm m_p)]\}\Big]G_2 \mp k^2\Big[5c_1\left(1+\frac{1}{s}c_\Lambda\right) - \frac{1}{s}c_k c_2 \pm d_\mp\Big\{c_1 + \left(1+\frac{1}{s}c_\Lambda\right)[\sqrt{s}(\sqrt{s}\pm m_p) - c_k]\Big\}\Big]G_3, \end{aligned} \tag{A15}$$

$$\begin{aligned} A_4 = {} & \mp\Big[5c_1 c_s + \frac{1}{s}c_k c_2 \mp d_\mp\{c_1(1+2c_\mp\sqrt{s}) \pm \sqrt{s}[c_s(\mp\sqrt{s} - m_p) \pm 2c_\mp c_1] + c_s c_k\}\Big]G_1 \\ & \pm\Big[5c_1\left(b_p - b_\Lambda + \frac{1}{s}k^2 c_\Lambda\right) + k^2 c_2\left(1 - \frac{1}{s}c_k\right) \pm d_\mp\{c_1[k^2 - \sqrt{s}(\sqrt{s}\pm m_p)] - (k^2 c_s - b_q) \\ & \times[\sqrt{s}(\sqrt{s}\pm m_p) - c_k]\}\Big]G_2 \pm k^2\Big[5c_1 c_s + \frac{1}{s}c_k c_2 \mp d_\mp\{c_1 - c_s[\sqrt{s}(\sqrt{s}\pm m_p) - c_k]\}\Big]G_3, \end{aligned} \tag{A16}$$

$$A_5 = \frac{1}{t-m_K^2}\Big(\Big[-5c_1(\sqrt{s}\pm m_p)\Big(\frac{3}{s}c_\Lambda+\frac{2c_1}{s-m_p^2}-1\Big)+c_2c_5c_\mp\Big(\frac{1}{s}c_k-2\Big)\pm d_\mp\Big\{(2+c_s)(b_p\sqrt{s}\pm m_pc_k)$$
$$-2c_\mp[c_1\Big(4b_p+\frac{3}{2}k^2\Big)+b_p(3c_1+2b_pc_s+2b_q)\pm 4m_p(b_pc_s-b_q)]\Big\}\Big]G_1+\Big[-5c_1(\sqrt{s}\pm m_p)$$
$$\times\{b_p+b_\Lambda-\frac{1}{s}c_\Lambda c_5\}-c_2c_5(\sqrt{s}\pm m_p)\Big(\frac{1}{s}c_k-1\Big)+d_\mp\{c_1c_5m_p\pm\sqrt{s}[(4b_pc_s-2b_p-b_q)b_p$$
$$+k^2b_pc_s]+c_km_p(c_5c_s-2b_p-b_q)\}\Big]G_2+\Big[-5c_1(\sqrt{s}\pm m_p)\Big\{4\Big(\frac{1}{s}b_pc_\Lambda-b_\Lambda\Big)$$
$$+k^2\Big(1+\frac{1}{s}c_\Lambda\Big)\Big\}+\frac{1}{s}c_kc_2c_5(\sqrt{s}\pm m_p)\mp d_\mp\{c_1c_5(\sqrt{s}\pm m_p)-b_p\sqrt{s}[4(b_q-b_pc_s)$$
$$-k^2(c_s+2)]\pm c_km_p[(2+c_s)k^2+4(b_pc_s-b_q)]\}\Big]G_3\Big), \tag{A17}$$

$$A_6 = \pm\Big[5c_1c_s+c_2\Big(\frac{1}{s}c_k-2\Big)\pm d_\mp c_\mp\{c_1(\sqrt{s}\pm m_p)+2c_1\sqrt{s}+c_s[c_k(\sqrt{s}\pm m_p)-k^2\sqrt{s}]\}\Big]G_1$$
$$\mp\Big[5c_1\Big(b_p+b_\Lambda-\frac{1}{s}c_\Lambda c_4\Big)+c_2(s-m_p^2)\Big(\frac{1}{s}c_k-1\Big)+d_\mp\{c_1(\sqrt{s}\pm m_p)m_p\pm[\sqrt{s}(\sqrt{s}\pm m_p)-c_k]$$
$$\times[(s-m_p^2)c_s-b_q]\}\Big]G_2\mp\Big[5c_1\Big[k^2-2b_\Lambda+\frac{1}{s}c_\Lambda c_4\Big]-\frac{1}{s}c_kc_2(s-m_p^2)\mp d_\mp\{c_1(\sqrt{s}\pm m_p)^2+[\sqrt{s}$$
$$\times(\sqrt{s}\pm m_p)-c_k][(s-m_p^2)c_s-2b_q]\}\Big]G_3, \tag{A18}$$

where

$$G_1 = \frac{ig_{K\Lambda N^*}g^a_{N^*p\gamma}}{10m^3_{N^*}(s-m^2_{N^*}+im_{N^*}\Gamma_{N^*})}, \tag{A19}$$

$$G_2 = \frac{ig_{K\Lambda N^*}g^b_{N^*p\gamma}c_\mp^2}{10m^3_{N^*}(s-m^2_{N^*}+im_{N^*}\Gamma_{N^*})}, \tag{A20}$$

$$G_3 = \frac{ig_{K\Lambda N^*}g^c_{N^*p\gamma}c_\mp^2}{10m^3_{N^*}(s-m^2_{N^*}+im_{N^*}\Gamma_{N^*})}. \tag{A21}$$

As in the case of spin $3/2$, the definition of G_1 here is slightly different from that in Eq. (31), i.e., $G_1 = \mathcal{G}_1k^2$, whereas $G_2 = \mathcal{G}_2$ and $G_3 = \mathcal{G}_3$. Here, the fitted coupling constants are

$$G^{(1)}_{N^*} \equiv g_{K\Lambda N^*}g^a_{N^*p\gamma}, \tag{A22}$$

$$G^{(2)}_{N^*} \equiv g_{K\Lambda N^*}g^b_{N^*p\gamma}, \tag{A23}$$

$$G^{(3)}_{N^*} \equiv g_{K\Lambda N^*}g^c_{N^*p\gamma}, \tag{A24}$$

and only $G^{(1)}_{N^*}$ and $G^{(2)}_{N^*}$ are relevant to the photoproduction process. Furthermore, in the formulation of both spin $3/2$ and $5/2$, we have used the following definitions:

$$b_p = p\cdot k = \frac{1}{2}(s-k^2-m_p^2), \tag{A25}$$

$$b_\Lambda = p_\Lambda\cdot k = \frac{1}{2}(k^2+m_\Lambda^2-u), \tag{A26}$$

$$b_q = q\cdot k = \frac{1}{2}(k^2+m_K^2-t), \tag{A27}$$

$$c_\Lambda = (p+k)\cdot p_\Lambda, \tag{A28}$$

$$c_k = (p+k)\cdot k, \tag{A29}$$

$$c_s = 1-\frac{1}{s}c_\Lambda, \tag{A30}$$

$$c_1 = b_\Lambda-\frac{1}{s}c_\Lambda c_k, \tag{A31}$$

$$c_2 = m_\Lambda^2-\frac{1}{s}c_\Lambda^2, \tag{A32}$$

$$c_3 = \frac{1}{s}c_k^2-k^2, \tag{A33}$$

$$c_4 = 2b_p+k^2, \tag{A34}$$

$$c_5 = 4b_p+k^2, \tag{A35}$$

$$c_\pm = \frac{1}{\sqrt{s} \pm m_p}, \tag{A36}$$

$$d_\pm = \frac{1}{s}(m_\Lambda \sqrt{s} \pm c_\Lambda). \tag{A37}$$

With an additional definition of $c_p = s - c_k$, the above definitions will also be used in the formulas of spin-3/2 and $-5/2$ resonances of Model 2.

APPENDIX B: SPIN-3/2 AND –5/2 RESONANCE AMPLITUDES FOR MODEL 2

1. Amplitudes for the spin-3/2 resonance

$$\begin{aligned} A_1 = {} & m_p\left[\left\{\frac{1}{2}(m_p+m_\Lambda)(c_\Lambda - m_\Lambda m_p - 3sc_s) + m_\Lambda(2sc_s - c_k)\right\} \pm m_{N^*}\left\{\frac{1}{2}(m_p+m_\Lambda)\right.\right. \\ & \left.\times\left(m_\Lambda - 3m_p c_s - \frac{1}{s}c_\Lambda m_p\right) + 2c_\Lambda - 2m_\Lambda^2 - 3c_1 - \frac{1}{s}c_\Lambda c_k\right\}\Bigg]G_1 + \Bigg[\left\{\frac{1}{2}(m_p+m_\Lambda)[m_p c_\Lambda \\ & + m_\Lambda(k^2-s)] + b_p c_\Lambda\right\} \pm m_{N^*}\left\{m_\Lambda b_p + \frac{1}{2}(m_p+m_\Lambda)\left[3(c_1 - b_p c_s) + \frac{1}{s}c_\Lambda(k^2-s)\right.\right. \\ & \left.\left.+ m_\Lambda m_p\right]\right\}\Bigg]G_2 + 2\{(b_p c_\Lambda - c_k m_\Lambda^2 - 3sc_1) \pm m_{N^*} m_\Lambda(c_k c_s - 3c_1 - k^2)\}G_3, \end{aligned} \tag{B1}$$

$$\begin{aligned} A_2 = {} & \frac{1}{t-m_k^2}\left(m_p\left[m_\Lambda k^2 \pm m_{N^*}\left\{3(k^2 - 2b_q) - \frac{2}{s}c_\Lambda k^2\right\}\right]G_1 + \left[\{3s(c_1 - b_p c_s) - m_\Lambda m_p k^2\}\right.\right. \\ & \left.\left.\pm m_{N^*} m_p\left\{3(b_p c_s - c_1) - \frac{1}{s}c_\Lambda k^2\right\}\right]G_2 + 4k^2(c_\Lambda \pm m_{N^*} m_\Lambda)G_3\right), \end{aligned} \tag{B2}$$

$$\begin{aligned} A_3 = {} & \frac{1}{2}m_p\left[3s - m_\Lambda m_p \pm m_{N^*}\{3(m_p - m_\Lambda) + \frac{2}{s}c_\Lambda m_p\}\right]G_1 + \frac{1}{2}\left[\{m_p c_\Lambda + m_\Lambda(k^2-s)\}\right. \\ & \left.\pm m_{N^*}\left\{m_\Lambda m_p + \frac{1}{s}c_\Lambda(k^2-s) + 3\left[c_1 + b_p\left(1 + \frac{1}{s}c_\Lambda\right)\right]\right\}\right]G_2 - 2\left\{m_\Lambda c_k \pm m_{N^*}\left(3c_1 + \frac{1}{s}c_\Lambda c_k\right)\right\}G_3, \end{aligned} \tag{B3}$$

$$\begin{aligned} A_4 = {} & -\frac{1}{2}m_p\left[\{3(c_\Lambda + sc_s) + m_\Lambda m_p\} \pm m_{N^*}\left\{3(m_p + m_\Lambda) - \frac{2}{s}m_p c_\Lambda\right\}\right]G_1 + \frac{1}{2}\left[\{m_p c_\Lambda + m_\Lambda(k^2-s)\}\right. \\ & \left.\pm m_{N^*}\left\{m_\Lambda m_p + \frac{1}{s}c_\Lambda(k^2-s) + 3(c_1 - b_p c_s)\right\}\right]G_2 - 2\left\{m_\Lambda c_k \pm m_{N^*}\left(3c_1 + \frac{1}{s}c_\Lambda c_k\right)\right\}G_3, \end{aligned} \tag{B4}$$

$$\begin{aligned} A_5 = {} & \frac{1}{t-m_k^2}\left(\frac{1}{2}m_p\left[-m_\Lambda c_5 \pm m_{N^*}\left\{3(k^2 - 2b_q) + \frac{2}{s}c_\Lambda c_5\right\}\right]G_1 + \frac{1}{2}\left[\left\{m_\Lambda m_p c_5 - 3s(c_1 + 3b_p c_s - 2b_p)\right\}\right.\right. \\ & \left.\left.\pm m_{N^*} m_p\left\{3(b_p + b_\Lambda) - \frac{2}{s}c_\Lambda c_5\right\}\right]G_2 - 2c_5(c_\Lambda \pm m_{N^*} m_\Lambda)G_3\right), \end{aligned} \tag{B5}$$

$$\begin{aligned} A_6 = {} & \frac{1}{2}m_p\left[\{m_\Lambda m_p + 3sc_s - c_\Lambda\} \pm m_{N^*}\left\{3m_p c_s + \frac{1}{s}m_p c_\Lambda - m_\Lambda\right\}\right]G_1 + \frac{1}{2}\left[m_p\{c_\Lambda - m_p m_\Lambda\}\right. \\ & \left.\pm m_{N^*}\left\{3(c_1 + b_p c_s) - \frac{1}{s}c_\Lambda m_p^2 + m_p m_\Lambda\right\}\right]G_2 + 2\{m_p c_\Lambda - m_\Lambda s \pm m_{N^*}(m_p m_\Lambda - c_\Lambda)\}G_3, \end{aligned} \tag{B6}$$

where in this case

$$G_i = \frac{s g_i g_{K\Lambda N^*}}{3m_{N^*}^6(s - m_{N^*}^2 + i m_{N^*}\Gamma_{N^*})}, \tag{B7}$$

with $i = 1, 2, 3$, and

$$g_1 = -2ig^a_{N^*p\gamma} + 3ig^c_{N^*p\gamma} + g^d_{N^*p\gamma}, \tag{B8}$$

$$g_2 = -2ig^a_{N^*p\gamma} - g^b_{N^*p\gamma} + 2ig^c_{N^*p\gamma} - 2g^d_{N^*p\gamma}, \tag{B9}$$

$$g_3 = -ig^a_{N^*p\gamma} + ig^c_{N^*p\gamma}. \tag{B10}$$

Therefore, the fitted coupling constants for the spin-3/2 resonance of Model 2 are

$$G^{(1)}_{N^*} \equiv g_{K\Lambda N^*} g^a_{N^*p\gamma}, \tag{B11}$$

$$G^{(2)}_{N^*} \equiv g_{K\Lambda N^*} g^b_{N^*p\gamma}, \tag{B12}$$

$$G^{(3)}_{N^*} \equiv g_{K\Lambda N^*} g^c_{N^*p\gamma}, \tag{B13}$$

$$G^{(4)}_{N^*} \equiv g_{K\Lambda N^*} g^d_{N^*p\gamma}. \tag{B14}$$

However, different from the case of Model 1, in the case of Model 2, all coupling constants may contribute to the photoproduction process. Hence, in Model 2, we practically have two more parameters.

2. Amplitudes for the spin-5/2 resonance

$$\begin{aligned}
A_1 = {} & 4\Big[-s\Big\{5c_1^2 + c_2c_3 + 2c_1\Big(\frac{1}{s}c_k m_\Lambda^2 - \frac{1}{s}b_p c_\Lambda\Big)\Big\} \pm m_{N^*}m_\Lambda\Big\{5c_1^2 + c_2c_3 + 2c_1\Big(\frac{1}{s}c_k c_\Lambda - b_p\Big)\Big\}\Big]G_1 \\
& + \Big[\{(m_p + m_\Lambda)c_1(sm_\Lambda - m_\Lambda k^2 - c_\Lambda m_p) - 2c_\Lambda b_p c_1 + (c_1 - b_p c_s)(m_p + m_\Lambda)(c_p m_\Lambda \\
& - c_\Lambda m_p)\} \pm m_{N^*}\{(c_1 - b_p c_s)(m_p + m_\Lambda)\Big(5c_1 - \frac{1}{s}c_p c_\Lambda + m_p m_\Lambda\Big) + (m_p + m_\Lambda)c_1 \\
& \times (m_\Lambda m_p - c_\Lambda) + \frac{1}{s}k^2(m_p + m_\Lambda)(c_1 c_\Lambda - c_p c_2) + 2b_p m_\Lambda c_1)\}\Big]G_2 + m_p[\{(m_p + m_\Lambda)[5sc_1c_s \\
& + c_k c_2 + m_p m_\Lambda(c_1 + c_k c_s) - c_\Lambda(c_1 + b_p c_s)] + 2m_\Lambda c_1(2c_k - 3sc_s)\} \pm m_{N^*}\Big\{(m_p + m_\Lambda) \\
& \times \Big[-m_p\Big(5c_1c_s + \frac{1}{s}c_k c_2\Big) + c_1\Big(m_\Lambda - \frac{1}{s}m_p c_\Lambda\Big) + c_s\Big(b_p m_\Lambda - \frac{1}{s}c_k c_\Lambda m_p\Big)\Big] - (10c_1^2 + 2c_2c_3) \\
& + 6c_1(c_\Lambda - m_\Lambda^2) - \frac{4}{s}c_k c_\Lambda c_1\Big\}\Big]G_3,
\end{aligned} \tag{B15}$$

$$\begin{aligned}
A_2 = {} & \frac{1}{t - m_k^2}\Big(16[c_1c_\Lambda k^2 \mp m_{N^*}c_1k^2m_\Lambda]G_1 + 2\Big[s\Big\{(b_pc_s - c_1)\Big(5c_1 - \frac{1}{s}c_k m_p m_\Lambda + \frac{1}{s}c_\Lambda b_p\Big) \\
& + \frac{1}{s}k^2(c_pc_2 + c_1m_pm_\Lambda)\Big\} \pm m_{N^*}\Big\{(b_pc_s - c_1)\Big(5c_1m_p + \frac{1}{s}c_kc_\Lambda m_p - b_pm_\Lambda\Big) + \frac{1}{s}m_pk^2(c_pc_2 \\
& - c_1c_\Lambda)\Big\}\Big]G_2 + 2m_p\Big[-\{k^2m_\Lambda c_1 + 2c_km_\Lambda(c_1 - b_pc_s) + k^2c_s(c_pm_\Lambda + c_\Lambda m_p)\} \pm m_{N^*}\Big\{2(c_1 \\
& - b_pc_s)\Big(5c_1 + \frac{1}{s}c_kc_\Lambda\Big) + k^2c_s\Big(\frac{1}{s}c_pc_\Lambda + m_\Lambda m_p - 5c_1\Big) \\
& + k^2\Big(\frac{1}{s}c_1c_\Lambda - \frac{1}{s}c_2c_p - c_2\Big)\Big\}\Big]G_3\Big),
\end{aligned} \tag{B16}$$

$$A_3 = 4\left[-2c_1c_km_\Lambda \pm m_{N^*}\left(5c_1^2 + c_2c_3 + \frac{2}{s}c_kc_\Lambda c_1\right)\right]G_1 + \left[s\left\{c_1\left(m_\Lambda - \frac{1}{s}k^2m_\Lambda - \frac{1}{s}c_\Lambda m_p\right) + \left(c_1 + b_p \times \left[1 + \frac{1}{s}c_\Lambda\right]\right)\left(\frac{1}{s}c_pm_\Lambda - \frac{1}{s}c_\Lambda m_p\right)\right\} \pm m_{N^*}\left\{\left(c_1 + b_p\left[1 + \frac{1}{s}c_\Lambda\right]\right)\left(5c_1 - \frac{1}{s}c_pc_\Lambda + m_pm_\Lambda\right) + \frac{1}{s}k^2 \times (c_\Lambda c_1 - c_pc_2) + c_1(m_pm_\Lambda - c_\Lambda)\right\}\right]G_2 + m_p\left[\left\{\left(1 + \frac{1}{s}c_\Lambda\right)(c_\Lambda b_p - m_pm_\Lambda c_k - 5sc_1) + c_kc_2 + c_1(5c_\Lambda + m_pm_\Lambda)\right\} \pm m_{N^*}\left\{\left(1 + \frac{1}{s}c_\Lambda\right)\left(5c_1m_p + \frac{1}{s}c_kc_\Lambda m_p - b_pm_\Lambda\right) - \frac{1}{s}c_kc_2m_p - c_1\left(\frac{1}{s}c_\Lambda m_p + 5m_\Lambda\right)\right\}\right]G_3, \tag{B17}$$

$$A_4 = 4\left[-2c_1c_km_\Lambda \pm m_{N^*}\left(5c_1^2 + c_2c_3 + \frac{2}{s}c_kc_\Lambda c_1\right)\right]G_1 + \left[s\left\{c_1\left(m_\Lambda - \frac{1}{s}k^2m_\Lambda - \frac{1}{s}c_\Lambda m_p\right) + (c_1 - b_pc_s) \times \left(\frac{1}{s}c_pm_\Lambda - \frac{1}{s}c_\Lambda m_p\right)\right\} \pm m_{N^*}\left\{(c_1 - b_pc_s)\left(5c_1 - \frac{1}{s}c_pc_\Lambda + m_pm_\Lambda\right) + \frac{1}{s}k^2(c_\Lambda c_1 - c_pc_2) + c_1(m_pm_\Lambda - c_\Lambda)\right\}\right]G_2 + m_p\left[\{-c_s(c_\Lambda b_p - m_pm_\Lambda c_k - 5sc_1) + c_kc_2 + c_1(5c_\Lambda + m_pm_\Lambda)\} \mp m_{N^*}\left\{c_s\left(5c_1m_p + \frac{1}{s}c_kc_\Lambda m_p - b_pm_\Lambda\right) + \frac{1}{s}c_kc_2m_p + c_1\left(\frac{1}{s}c_\Lambda m_p + 5m_\Lambda\right)\right\}\right]G_3, \tag{B18}$$

$$A_5 = \frac{1}{t - m_k^2}\left(8c_1c_5[-c_\Lambda \pm m_{N^*}m_\Lambda]G_1 + \left[\left\{\left(b_p + b_\Lambda - \frac{1}{s}c_\Lambda c_5\right)(5sc_1 - c_km_pm_\Lambda + c_\Lambda b_p) - c_5(c_pc_2 + c_1m_pm_\Lambda)\right\} \pm m_{N^*}\left\{\left(b_p + b_\Lambda - \frac{1}{s}c_\Lambda c_5\right)\left(5c_1m_p + \frac{1}{s}c_kc_\Lambda m_p - b_pm_\Lambda\right) - \frac{1}{s}m_pc_5(c_pc_2 - c_1c_\Lambda)\right\}\right]G_2 + m_p\left[\left\{c_5m_\Lambda c_1 + 2c_km_\Lambda\left(b_p + b_\Lambda - \frac{1}{s}c_\Lambda c_5\right) + \left(4b_\Lambda - k^2 - \frac{1}{s}c_\Lambda c_5\right)(c_pm_\Lambda + c_\Lambda m_p)\right\} \mp m_{N^*}\left\{2\left(b_p + b_\Lambda - \frac{1}{s}c_\Lambda c_5\right)\left(5c_1 + \frac{1}{s}c_kc_\Lambda\right) + \left(4b_\Lambda - k^2 - \frac{1}{s}c_\Lambda c_5\right)\left(\frac{1}{s}c_pc_\Lambda + m_\Lambda m_p - 5c_1\right) + c_5\left(\frac{1}{s}c_1c_\Lambda - \frac{1}{s}c_2c_p - c_2\right)\right\}\right]G_3\right), \tag{B19}$$

$$A_6 = 8c_1[c_\Lambda m_p - sm_\Lambda \pm m_{N^*}(c_\Lambda - m_pm_\Lambda)]G_1 + \left[c_1m_p(m_pm_\Lambda - c_\Lambda) + (c_1 + b_pc_s)(c_pm_\Lambda - m_pc_\Lambda) \pm m_{N^*}\left\{(c_1 + b_pc_s)\left(5c_1 - \frac{1}{s}c_pc_\Lambda + m_pm_\Lambda\right) + \frac{1}{s}c_4(c_1c_\Lambda - c_pc_2) + c_1(m_pm_\Lambda - c_\Lambda)\right\}\right]G_2 + m_p\left[\{c_s(b_pc_\Lambda - m_pm_\Lambda c_k - 5sc_1) + c_2(2s - c_k) + c_1(3c_\Lambda - m_pm_\Lambda)\} \pm m_{N^*} \times \left\{c_s\left(5c_1m_p + \frac{1}{s}m_pc_kc_\Lambda - b_pm_\Lambda\right) + c_1\left(\frac{1}{s}m_pc_\Lambda - 3m_\Lambda\right) - \left(2 - \frac{1}{s}c_k\right)m_pc_2\right\}\right]G_3. \tag{B20}$$

Similar to the spin-3/2 case, here we have

$$G_i = \frac{s^2g_ig_{K\Lambda N^*}}{10m_{N^*}^{10}(s - m_{N^*}^2 + im_{N^*}\Gamma_{N^*})}, \tag{B21}$$

with $i = 1, 2, 3$, and

$$g_1 = ig^a_{N^*p\gamma} - ig^c_{N^*p\gamma}, \tag{B22}$$

$$g_2 = -2ig^a_{N^*p\gamma} - g^b_{N^*p\gamma} + 2ig^c_{N^*p\gamma} - 2g^d_{N^*p\gamma}, \tag{B23}$$

$$g_3 = -2ig^a_{N^*p\gamma} + 3ig^c_{N^*p\gamma} + g^d_{N^*p\gamma}. \tag{B24}$$

As in the case of spin-3/2 resonance, here the fitted coupling constants for the spin-5/2 resonances in Model 2 read

$$G^{(1)}_{N^*} \equiv g_{K\Lambda N^*} g^a_{N^*p\gamma}, \tag{B25}$$

$$G^{(2)}_{N^*} \equiv g_{K\Lambda N^*} g^b_{N^*p\gamma}, \tag{B26}$$

$$G^{(3)}_{N^*} \equiv g_{K\Lambda N^*} g^c_{N^*p\gamma}, \tag{B27}$$

$$G^{(4)}_{N^*} \equiv g_{K\Lambda N^*} g^d_{N^*p\gamma}, \tag{B28}$$

where all coupling constants contribute to the photoproduction process.

[1] H. Kamano, S. X. Nakamura, T.-S. H. Lee, and T. Sato, Phys. Rev. C **88**, 035209 (2013).

[2] X. Cao, V. Shklyar, and H. Lenske, Phys. Rev. C **88**, 055204 (2013); B. Julia-Diaz, B. Saghai, T.-S. H. Lee, and F. Tabakin, Phys. Rev. C **73**, 055204 (2006); E. Klempt, A. V. Anisovich, V. A. Nikonov, A. V. Sarantsev, and U. Thoma, Eur. Phys. J. A **29**, 307 (2006); V. Shklyar, H. Lenske, and U. Mosel, Phys. Rev. C **72**, 015210 (2005); W. T. Chiang, B. Saghai, F. Tabakin, and T. S. H. Lee, Phys. Rev. C **69**, 065208 (2004); T. Feuster and U. Mosel, Phys. Rev. C **59**, 460 (1999); N. Kaiser, T. Waas, and W. Weise, Nucl. Phys. **A612**, 297 (1997).

[3] T. Mart and C. Bennhold, Phys. Rev. C **61**, 012201 (1999).

[4] T. Mart, Phys. Rev. D **83**, 094015 (2011).

[5] T. Mart, Phys. Rev. D **88**, 057501 (2013); *Proc. Sci.*, Hadron 2013 (2013) 144; Few Body Syst. **54**, 311 (2013); AIP Conf. Proc. **1454**, 19 (2011).

[6] Z. Li, H. Ye, and M. Lu, Phys. Rev. C **56**, 1099 (1997); R. Koniuk and N. Isgur, Phys. Rev. D **21**, 1868 (1980).

[7] K. A. Olive *et al.* (Particle Data Group Collaboration), Chin. Phys. C **38**, 090001 (2014).

[8] T. Mart and B. I. S. van der Ventel, Phys. Rev. C **78**, 014004 (2008); T. Mart, Nucl. Phys. **A815**, 18 (2009); T. Mart, L. Tiator, D. Drechsel, and C. Bennhold, Nucl. Phys. **A640**, 235 (1998); **631**, 765 (1998).

[9] A. Salam, T. Mart, and K. Miyagawa, Few Body Syst. **54**, 261 (2013); K. Miyagawa, T. Mart, C. Bennhold, and W. Glockle, Phys. Rev. C **74**, 034002 (2006); H. Yamamura, K. Miyagawa, T. Mart, C. Bennhold, W. Glöckle, and H. Haberzettl, Phys. Rev. C **61**, 014001 (1999).

[10] S. Sumowidagdo and T. Mart, Phys. Rev. C **60**, 028201 (1999); T. Mart, Few Body Syst. **42**, 125 (2008); Int. J. Mod. Phys. A **23**, 599 (2008).

[11] L. De Cruz, T. Vrancx, P. Vancraeyveld, and J. Ryckebusch, Phys. Rev. Lett. **108**, 182002 (2012); L. De Cruz, J. Ryckebusch, T. Vrancx, and P. Vancraeyveld, Phys. Rev. C **86**, 015212 (2012).

[12] R. A. Adelseck, C. Bennhold, and L. E. Wright, Phys. Rev. C **32**, 1681 (1985).

[13] J.-C. David, C. Fayard, G. H. Lamot, and B. Saghai, Phys. Rev. C **53**, 2613 (1996).

[14] W. Rarita and J. Schwinger, Phys. Rev. **60**, 61 (1941).

[15] P. A. Moldauer and K. M. Case, Phys. Rev. **102**, 279 (1956); L. M. Nath, B. Etemadi, and J. D. Kimel, Phys. Rev. D **3**, 2153 (1971); H. T. Williams, Phys. Rev. C **31**, 2297 (1985); H. Haberzettl, arXiv:nucl-th/9812043.

[16] V. Pascalutsa, Phys. Rev. D **58**, 096002 (1998).

[17] M. Benmerrouche, R. M. Davidson, and N. C. Mukhopadhyay, Phys. Rev. C **39**, 2339 (1989).

[18] T. Mizutani, C. Fayard, G. H. Lamot, and B. Saghai, Phys. Rev. C **58**, 75 (1998).

[19] O. V. Maxwell, Phys. Rev. C **70**, 044612 (2004).

[20] T. Vrancx, L. De Cruz, J. Ryckebusch, and P. Vancraeyveld, Phys. Rev. C **84**, 045201 (2011).

[21] V. Pascalutsa, Phys. Lett. B **503**, 85 (2001).

[22] V. Pascalutsa and R. Timmermans, Phys. Rev. C **60**, 042201 (1999).

[23] B. B. Deo and A. K. Bisoi, Phys. Rev. D **9**, 288 (1974).

[24] P. Dennery, Phys. Rev. **124**, 2000 (1961).

[25] J. D. Bjorken and S. D. Drell, *Relativistic Quantum Mechanics* (McGraw-Hill, New York, 1964).

[26] A. Donnachie, *High Energy Physics*, edited by E. H. S. Burhop (Academic Press, New York, 1972), Vol. 5, p. 1.

[27] E. Amaldi, S. Fubini, and G. Furlan, *Pion-Electroproduction* (Springer-Verlag, Heidelberg, 1979).

[28] G. Knöchlein, D. Drechsel, and L. Tiator, Z. Phys. A **352**, 327 (1995).

[29] T. Mart and A. Sulaksono, Phys. Rev. C **74**, 055203 (2006).

[30] T. Mart, Phys. Rev. C **82**, 025209 (2010).

[31] T. Mart and M. J. Kholili, Phys. Rev. C **86**, 022201(R) (2012).

[32] T. Mart and N. Nurhadiansyah, Few-Body Syst. **54**, 1729 (2013).

[33] T. Mart and A. K. Sari, Mod. Phys. Lett. A **28**, 1350054 (2013).

[34] T. Mart, Phys. Rev. C **87**, 042201(R) (2013).

[35] L. Syukurilla and T. Mart, Int. J. Mod. Phys. E **24**, 1550008 (2015); AIP Conf. Proc. **1617**, 126 (2014).

[36] T. Mart, Phys. Rev. C **90**, 065202 (2014).

[37] H. Haberzettl, C. Bennhold, T. Mart, and T. Feuster, Phys. Rev. C **58**, R40 (1998).

[38] J. M. Laget, Nucl. Phys. **A481**, 765 (1988).
[39] V. Shklyar, H. Lenske, and U. Mosel, Phys. Rev. C **82**, 015203 (2010).
[40] F. X. Lee, T. Mart, C. Bennhold, H. Haberzettl, and L. E. Wright, Nucl. Phys. **A695**, 237 (2001).
[41] R. Bradford *et al.* (CLAS Collaboration), Phys. Rev. C **73**, 035202 (2006).
[42] M. E. McCracken *et al.* (CLAS Collaboration), Phys. Rev. C **81**, 025201 (2010).
[43] M. Sumihama *et al.* (LEPS Collaboration), Phys. Rev. C **73**, 035214 (2006).
[44] K. Hicks *et al.*, Phys. Rev. C **76**, 042201 (2007).
[45] T. C. Jude *et al.* (Crystal Ball at MAMI Collaboration), Phys. Lett. B **735**, 112 (2014).
[46] A. Lleres *et al.* (GRAAL Collaboration), Eur. Phys. J. A **31**, 79 (2007).
[47] R. Bradford *et al.*, Phys. Rev. C **75**, 035205 (2007).
[48] A. Lleres *et al.* (GRAAL Collaboration), Eur. Phys. J. A **39**, 149 (2009).
[49] K. H. Glander *et al.*, Eur. Phys. J. A **19**, 251 (2004).
[50] R. A. Adelseck and B. Saghai, Phys. Rev. C **42**, 108 (1990); **45**, 2030 (1992).
[51] P. Bydžovský (private communication). The conclusion drawn on the results of using different spin-3/2 prescriptions in the present work is consistent with his result.
[52] D. Diakonov, V. Petrov, and M. Polyakov, Z. Phys. A **359**, 305 (1997).
[53] R. Schumacher, *Proceedings of the 9th International Conference on Hypernuclear and Strange Particle Physics (HYP 2006), Mainz, Germany, 2006*, edited by J. Pochodzalla and T. Walcher (University of Mainz, Germany, 2007), p. 339.
[54] D. Drechsel and L. Tiator, J. Phys. G **18**, 449 (1992).
[55] S. Steininger and U. G. Meissner, Phys. Lett. B **391**, 446 (1997).
[56] T. Mart, Phys. Rev. C **83**, 048203 (2011).
[57] M. K. Cheoun, B. S. Han, B. G. Yu, and I. T. Cheon, Phys. Rev. C **54**, 1811 (1996).
[58] V. Shklyar, H. Lenske, and U. Mosel, Phys. Rev. C **87**, 015201 (2013).
[59] A. V. Anisovich, R. Beck, E. Klempt, V. A. Nikonov, A. V. Sarantsev, and U. Thoma, Eur. Phys. J. A **48**, 15 (2012).
[60] Further information about the Jefferson Lab Frozen Spin Target (FroST) experiment can be found at http://www.jlab.org/~ckeith/Frozen/Frozen.html.
[61] Berends, A. Donnachie, and D. L. Weaver, Nucl. Phys. **B4**, 1 (1967).
[62] T. Mart, Ph. D. Thesis, University of Mainz, 1996 (unpublished).
[63] http://www.kph.uni-mainz.de/MAID/kaon/kaonmaid.html.
[64] http://pwa.hiskp.uni-bonn.de/.